NTNU
Norwegian University of
Science and Technology

Corrosion Behaviour of Aluminium-Steel Welded Joints

Fredrik Heggeset Tranø

Materials Technology (MIMT)
Submission date: June 2018
Supervisor: Trond Furu, IMA
Co-supervisor: Otto Lunder, SINTEF

Norwegian University of Science and Technology
Department of Materials Science and Engineering

Preface

This master thesis is written at the Department of Material Science and Engineering at the Norwegian University of Science and Technology (NTNU). With a duration of 20 weeks in the spring of 2018, this work finalizes the two-year master's degree program in Material Science and Engineering.

The master project is linked with the OPTIMALS research project (Optimal design and production of lightweight and high-performance aluminium-steel structural components) where Benteler Automotive, Hydro and HyBond are industrial partners and SINTEF Materials and Chemistry is the R&D partner. The main goal of this project is to enable multi-material solutions for high-performance aluminium-steel structural components with the goal to reduce both weight and manufacturing cost in the automotive industry. The project is also a part of the NAPIC Centre (NTNU Aluminium product Innovation Centre), whose vision is to find new product areas for aluminium and to establish NTNU as a world leader in the application of aluminium products.

Trondheim, June 8, 2018

Fredrik H. Tranø

Acknowledgement

I would like to acknowledge my supervisors, Professor Trond Furu[1] and Professor Otto Lunder[2], for help and guidance during this project work.

Much appreciation also goes to Professor Øystein Grong[3], OPTIMALS project leader Xiaobo Ren[2] and Ragnhild Aune[2] who has provided valuable wisdom and advice during this master project.

A special thanks goes to Ph.D.-candidate Catalina H. M. Hagen[2] who made it possible to conduct the Scanning Kelvin Probe analysis, provided valuable information and interpreted the results from the analysis.

Finally, I would like to thank Department Engineer Trygve Lindahl Schanche[4], Department Engineer Pål Christian Skaret[4], Senior Engineer Yingda Yu[4] and Department Engineer Anita Storsve[4] for providing knowledge, help and training in the metallography, tensile testing, SEM and corrosion laboratories.

[1]Hydro Aluminium, Sunndalsøra
[2]SINTEF, Materials and Nanotechnology, Trondheim
[3]HyBond AS, Trondheim
[4]Department of Material Science and Engineering, NTNU, Trondheim

Abstract

Multi-material solutions is a hot research topic in the automotive industry. The possibility to combine the physical and mechanical properties of different materials in a car component can both increase passenger safety, weight and thus the fuel economy of cars in the future. The combination of steel and aluminium in car components can offer a better combination of structural integrity, impact resistance and weight savings compared to components made entirely from steel. In practice, suitable components such as the B-pillar, bumper and battery housing in electric vehicles, will be changed to aluminium. Steel brackets will then need to be joined to the aluminium which then again can be joined to the rest of the car's body.

The development of multi-material solutions in high-performance automotive components is accelerating the development of existing welding methods and also the invention of entirely new methods. Welding of dissimilar metals is a complex task due to potentially large differences in physical and mechanical properties and the demand for precision control and tailoring of weld parameters is high to achieve joints with superior mechanical properties. Aluminium-steel joints have already been used in the automotive industry, but the majority of the research published on this subject aims to improve mechanical properties while studies of the corrosion properties of such joints are reported more rarely.

In this project, two different heat-treatable aluminium alloys, AA6063 and AA6082, were joined to a zinc coated dual phase steel, HCT600, by a fusion welding method named Cold Metal Transfer. The materials and the welding method used in this project are relevant for automotive application. Prior to welding, the aluminium alloys were heat treated to an under-aged and a peak-aged temper condition referred to as T6x and T6, respectively. Four different material combinations were welded and Vickers hardness measurements were conducted to verify that the respective temper conditions were reached and to evaluate the effect of welding on hardness. After welding, tensile test specimens were prepared and subjected to an immersion corrosion test with acidified salt water as electrolyte. Tensile tests were performed before, during and after the corrosion test to evaluate the effect of corrosion versus time on the mechanical strength of such joints. In addition, metallographic and electrochemical examinations were carried out by the use of Light Optical Microscopy (LOM), Scanning Electron Microscopy (SEM) and Scanning Kelvin Probe (SKP) analysis were used to asses the materials both before and after corrosion.

Results revealed that the zinc coating, originally applied to the steel for corrosion protection and better wetting during welding, is causing the formation of zinc rich zones and phases in the filler material. These zones and phases corroded fast in the corrosive environment. Subsequently, this proved to be detrimental to the bond strength of such joints. Hybrid Metal Extrusion and Bonding (HYB) is a new solid-state joining method developed by HyBond AS. This method is showing promising results in the joining of such joints without the use of zinc in the fusion zone. The test procedure performed in this work should be used to test HYB joints of the same materials when samples are ready for corrosion testing.

Sammendrag

Løsninger for å kombinere ulike material i bilkomponenter er et viktig forskningstema for bilindustrien. Muligheten til å kombinere de fysiske og mekaniske egenskapene fra ulike materialer i en komponent kan føre til forbedringer i passasjersikkerhet, vekt og dermed også drivstoffeffektivitet i fremtidens biler. Kombinasjonen av stål og aluminium er spesielt interessant i bilkomponenter og kan gi bedre strukturell integritet, kollisjonsmotstand og vektbesparelser sammenlignet med komponenter som kun er laget stål. I praksis vil stålbraketter festes til komponenter som er aktuelle for å lages i aluminium, som for eksempel B-pilar, støtfanger og batterikasse i elektriske biler. Disse stålbrakettene vil videre bli satt sammen med resten av bilkarosseriet.

Utviklingen av multi-materialløsninger for bruk i bilkomponenter er med på å sette fart i forbedring av eksisterende og utvikling av nye sveisemetoder. Sveising av ulike metaller til hverandre er en utfordrende oppgave på grunn av potensielt store forskjeller i fysiske og mekaniske egenskaper. Komponenter som kombinerer stål og aluminium er allerede tatt i bruk av bilindustrien, men majoriteten av forskning publisert rundt temaet har som mål å optimalisere mekaniske egenskaper mens studier på korrosjonsmotstand er sjeldnere rapportert.

I dette prosjektet har to utherdbare aluminiumslegeringer, AA6063 og AA6082, blitt sveist til et galvanisert tofase stål, HCT600, ved hjelp av en metode som heter ”Cold Metal Transfer”. Materialene og sveisemetoden som er benyttet er relevante opp mot bilindustrien. Før sveising ble aluminiumslegeringene herdet til undereldet tilstand og eldet til maksimal hardhet referert til som henholdsvis T6x- og T6-tilstand. Fire forskjellige materialkombinasjoner ble sveist og Vickers hardhetsmålinger ble brukt for å verifisere herdetilstanden og for å evaluere hvilken effekt sveising har på hardheten og styrken til til materialene. Videre ble strekkprøver maskinert og utsatt for en korrosjonstest ved neddykking i en forsuret saltvannsløsning. Strekkprøver ble gjennomført før, under og etter korrosjonsforsøket for å evaluere effekten korrosjon har på styrken til sammenføyningen over tid. I tillegg ble metallografiske og elektrokjemiske undersøkelser gjennomført ved hjelp av lysmikroskopi, scanning elektronmikroskopi og ”Scanning Kelvin Probe”-målinger.

Resultatene viste at sinken, som i utgangspunktet er påført stålet for å gi bedre korrosjonsbeskyttelse og fuktingsvinkel ved sveising, fører til dannelse av sinkrike soner og faser i tilsatsmaterialet. Disse sonene og fasene korroderte raskt i den korrosive løsningen. Dette førte til stort styrketap i bindingen mellom tilsatsmaterial av aluminium og stålplaten. ”Hybrid metal extrusion and bonding” (HYB) er en ny fast-fase sveisemetode utviklet av HyBond AS. Denne metoden har vist lovende resultater for sveising av stål og aluminium uten behov for sink i sveisesonen i motsetning til CMT. Testprosedyren som er gjennomført i dette arbeidet bør gjennomføres på HYB-sveiser når disse er tilgjengelige for korrosjonstesting.

Table of Contents

Chapter 1

Introduction

1.1 Background

Since the 1920s, steel has been the dominant material used in the automotive industry. The material selection process in the automotive industry is complex and determined by a number of factors. Government regulations impose the car manufacturers to reduce exhaust emissions, improve passenger safety and improve fuel efficiency. To meet these requirements, efforts are being made to improve conventional engine efficiency, develop hybrid powertrain systems and reduce vehicle weight. The properties of aluminium make it a good candidate to replace heavier materials in a car. Its high strength to weight ratio, good formability, good general corrosion resistance and recycling potential can be utilized to meet the demand for weight reduction in the industry [1, 2].

As an example of government imposed regulations. The Corporate Average Fuel Economy (CAFE) regulations in the United States sets high demands on the car manufacturers to improve fuel efficiency in cars. In essence, CAFE demands *"a doubling in fuel economy for light-duty vehicles by 2025"*[3]. This forces the car manufacturers to put an even higher focus on mass reduction. One of the most important research projects conducted in Europe is the Super Light Car (SLC) project from 2009. 37 partners and Volkswagen AG, as project manager, collaborated to achieve a 35 % weight reduction by the use of multi-material solutions in cars[4].

Multi-material solutions will be more and more relevant for a range of applications within both automotive industry and general engineering. In order to achieve optimal solutions for lightweight structural components, there is a need to combine different materials in multi-material solutions. In order to introduce multi-material structural components with high-performance requirements, such as aluminium-steel crash system components for the automotive industry, both the design principles and production processes need to be developed and industrialized. The key to success is a combination of component design, materials and joining technologies.

Vehicle development relies on developments in material, design and manufacturing technologies and only integrated solutions that work on these three key technologies will

be successful in the future. Material development of metals, light metals and also fibre reinforced plastic composites will play a major in vehicle development. In manufacturing, the development of joining technologies is especially important. Mechanical joining, adhesive and hybrid methods will play an important role, especially in multi-material solutions [4].

There are a lot of challenges connected to the joining of dissimilar metals. Existing processes are being improved and novel processes are being developed to improve product properties. A more comprehensive understanding of the processes is crucial to improve ductility, strength, robustness, performance, life-expectancy and automation. More knowledge is required on failure mechanisms and currently, there is a lack of standardization in terms of testing and characterization of dissimilar metal joints [5]. There is a growing interest in the research of aluminium-steel components. However, most studies are focused on improving the mechanical properties of such joints and studies of the corrosion properties are rarely reported [6].

The major problems associated with fusion welding of dissimilar metals are large heat input from the fusion welding process. The heat will lead to the formation of brittle intermetallic phases and softening of base materials in the Heat Affected Zone (HAZ). In this project two different welding techniques will be investigated, one fusion welding method and one solid-state joining method. Cold Metal Transfer (CMT) is a modified gas metal arc welding (GMAW) method developed to provide precision control of the process parameters for precision control of the mentioned heat input. This is why CMT is characterized as ”cold” compared to other GMAW techniques [1].

The Hybrid Metal Extrusion and Bonding (HYB) method is a novel solid-state joining method, invented by Professor Øystein Grong at NTNU and HyBond AS is a spin-off company from NTNU that has been founded to industrialize the method together with several industrial partners. HYB has been developed to eliminate the formation of a heat affected zone (HAZ) and thus the strength loss associated with the welding of aluminium [7]. Ongoing trials and research has resulted in successful joining aluminium and steel by the use of the HYB method.

1.2 Objectives of this thesis

In this project, two different aluminium alloys are going to be welded to steel by the use of CMT and HYB. Extruded plates of AA6063 and AA6082 in both under- and peak aged tempers are going to be welded by CMT to a zinc coated dual phase (DP) steel, HCT600, in a lap joint configuration. The same alloys are also going to be welded by the HYB method. Successful joints are going to be exposed to accelerated corrosion testing and material degradation will be quantified by the loss in mechanical strength through tensile testing. The goal of this work is to:

- Identify the optimal combination of aluminium alloy, temper condition and welding method in terms of corrosion resistance.
- Characterize corrosion attacks.
- Identify the cause of the corrosion attacks.

Chapter 2

Theoretical background

In this chapter, relevant literature is being presented, starting with the materials and their history of application in the automotive industry. The fundamentals of the applied welding methods and relevant corrosion mechanisms are presented. Finally, updated research on the corrosion of welded aluminium-steel joints is being reviewed.

2.1 Steel

Ferrous alloys are the most widespread engineering construction material in the world due to the abundant quantities of iron-containing compounds in the earth's crust, relatively low production costs and the versatility in terms of tailoring of mechanical and physical properties. Steels are alloys containing mainly iron and carbon and the carbon content is often governing the mechanical properties. Alloy steels are classified mainly after carbon content, but subclasses also exist according to the concentration of other alloying elements [8].

The most produced steels in the world are low-carbon steels, generally containing less than 0.25 wt% C. The microstructure consists of ferrite and pearlite giving alloys that are relatively soft and weak but have outstanding ductility and toughness. Also, good machinability, weldability and low production costs make low-carbon steels especially suitable for construction, structural components and automobile body components [8].

Strength in conventional steel grades is mainly achieved through solid solution strengthening by the addition of carbon and manganese. These steels have low toughness and are not suitable for modern applications. The toughness, which is measured by the ductile/brittle temperature, decreases with increasing carbon content. Also, high carbon contents lead to cracking during welding. Steels with low carbon content were then produced. The strength in these steels is achieved by grain size reduction. A fine-grained ferritic microstructure is produced by thermomechanically controlled processing (TMCP), which is controlled rolling in the austenitic region combined with continuous cooling. Further grain refinement is achieved through the addition of microalloying elements. Small concentrations (¡0.1 wt %) of niobium, titanium, vanadium and aluminium added to steels

with 0.03-0.008 %C and up to 1.5 wt% Mn, made it possible to produce steels with yield strengths between 450 - 550 MPa and a ductile/brittle transition temperature down to -70 $^{\circ}C$. These steels are known as High-Strength Low-Alloy (HSLA) steels [9].

The specific demands to the materials in the automotive industry are getting tougher. Up until the 1970's, the steel was cold rolled, primed and painted. This resulted in poor corrosion resistance and the solution to the corrosion problems was hot-dip galvanized steel. Extensive research on zinc coatings was initiated and by the 1980's galvanized steel became the standard for car manufacturers. In addition, pre-treatments such as phosphating and "e-coat" primers were developed to meet surface finish requirements [3].

Low-density materials have given the steel industry strong competition in the last 20 years. Increasing requirements in terms of passenger safety, vehicle performance and fuel economy have triggered a rapid development of high strength steels that can provide the same strength with less material. These steels are known as Advanced High Strength Steels (AHSS) and have improved formability and crash-worthiness compared to conventional steel grades [10].

2.1.1 Advanced High-Strength Steels (AHSS)

As the name implies, these steel grades are advanced compared to conventional steels. The properties of AHSS are a result of a multi-phase complex microstructure. The phase composition and distribution, volume fraction, size and morphology of the phase constituents are controlling the mechanical properties. Compared to conventional high strength steels, where increased strength leads to a decrease in ductility, a combination of high strength, formability and ductility are combined in AHSS[10, 11].

AHSS are multiphase steels that contain ferrite, bainite, martensite and retained austenite. The distribution and morphologies of these phases are precisely engineered to obtain certain mechanical properties [12]. The different types of AHHS are divided into dual phase (DP), complex phase (CP), transformation induced plasticity (TRIP), twinning induced plasticity (TWIP), hot formed (HF) and martensitic steels (MART) [10, 11]. These generic types are made to meet the performance demands of specific automotive parts. For example, DP and TRIP steels are used in crash zones and B-pillars of the car because of its high-energy absorption. For structural components, such as the passenger compartment, extremely high-strength MART steels are used to improve safety [11, 12].

Dual Phase Steels

HSLA steels offer improved strength to weight ratio compared to ordinary steels. The challenge with these steel types is that an increase in strength will reduce the ductility and thus, the formability. The demand for safety and fuel economy in the automotive industry has led to the development of steel types that are both strong and formable [9].

Dual phase (DP) steels are low alloy steels that have both high strength and ductility. Formability is the product of strength and uniform elongation and this is a particularly important parameter in the automotive industry. In addition to high strength and ductility, dual phase steels have properties such as continuous yielding and rapid strain hardening which is advantages for automotive use. DP steels consist of one soft and one significantly

harder phase, e.g. ferrite and martensite. The mechanical properties of DP steels are controlled by several parameters. Volume fraction, size, shape and distribution of the hard phase and grain size of the soft phase governs the mechanical properties of the steel. The dual phase microstructure is achieved through thermomechanical treatment and intercritical annealing [9, 13].

- Step 1: Thermomechanically controlled processing (TMCP) to produce a fully ferritic structure.
- Step 2: Intercritical annealing where the steel is heated into the $\alpha + \gamma$ region, between Ae_1 and Ae_3, typically at 790 $^{\circ}C$ for several minutes to form small regions of austenite in the ferrite. The austenite is then transformed to martensite upon sufficiently rapid cooling.

The addition of Mo to a steel that already contains Mn, the hardenability of the steel increases and martensite can be formed upon air cooling after intercritical annealing. It is also possible to avoid the extra step of intercritical annealing by addition of Cr and Mo. The desired dual phase microstructure then forms during cooling after controlled rolling [9].

The use of AHSS in automotive industry

The application of forming and welding is an integral part of automotive manufacturing and the welding of AHSS requires a different approach than that for low-carbon steel because of its complex microstructure. During welding with conventional techniques, the peak temperature of the fusion zone (FZ) is above the melting point of steel. This creates a Heat Affected Zone (HAZ) where significant austenite grain growth followed by phase transformation takes place. Consequently, the resulting microstructure is then different from the base material and thus, with different mechanical properties. The important goal is therefore to apply high precision control of the welding parameters to achieve optimal thermal conditions. Solid-state welding and alternative welding methods are implemented to preserve the functional properties of AHSS [12].

The Ultra-Light Steel Body program (ULSAB), that finished in 1995, was a collaboration project where 33 steel companies cooperated to research how steel could compete with low-density materials in terms of weight reduction and crash-worthiness. The project showed that through effective use of AHSS, body weight could be reduced by up to 25 %. After the ULSAB project, car manufacturers started to increase their use of AHSS. This often resulted in better crash-worthiness combined with a reduction in mass [3].

Another research project, the Future Steel Vehicle (FSV) program, expects that the mid-size cars of the future will contain 20 new types of AHSS. These steels are the newest in steel technology and of these steels, 30 % is expected to be DP steels with strengths ranging from 500 to 1000 MPa [13, 14].

2.2 Aluminium

Aluminium and aluminium alloys are characterized by its low density (2700 kg/m^3), high formability, good corrosion resistance in common environments and high specific

strength (tensile strength-specific gravity ratio). To reduce fuel consumption, transportation and automotive industry have started to apply aluminium alloys as engineering materials [8].

In its pure form, aluminium has relatively low strength. This is due to the high dislocation mobility in pure FCC-metals. In pure ferritic iron with its BCC structure, the dislocation mobility is lower, hence the greater strength. Alloying elements are added to aluminium to increase the strength through solid-solution strengthening or precipitation hardening. By the application of these strengthening mechanisms, aluminium alloys with strength comparable to many construction steels can be produced [15].

The price of aluminium is around twice the price of steel. However, the fuel efficiency can be increased and consequently, the environmental effect can be reduced by the use of aluminium. According to Fridlyander et.al. [16], if a reduction of 120 kg per car can be achieved by replacing aluminium with steel, 982 million liters of fuel can be saved and thus reduce CO_2 emissions by 2.3 million tonnes. This is based on a calculation for ten million cars with an average haulage of 15 thousand km per year. Also, proper modular design combined with the recycling potential of aluminium can help to solve the cost concern associated with the use of aluminium for the car manufacturers.

The aluminium alloys utilized in the automotive industry can be divided into non-heat treatable and heat treatable alloys. The most used non-heat treatable alloys are AlMn alloys (3xxx series) and AlMg alloys (5xxx series). The most used heat treatable alloys are AlCu alloys (2xxx series) and AlMgSi alloys (6xxx series) [16].

2.2.1 AlMgSi alloys

Aluminium alloys with Mg and Si as main alloying elements are referred to as AlMgSi alloys or 6xxx series of aluminium. These alloys are extensively used as extruded profiles and of the four million tonnes of extruded profiles produced in the world, half of these are produced as AlMgSi. The typical composition of AlMgSi alloys is Al-(0.5-1.3)%Mg-(0.4-1.4)%Si. In addition (0.5-0.7)%Mn and (0.1-0.3)%Cr are added for grain refinement and Cu(0.3-0.9%) for increased strength. However, a Cu-content above 0.5 % has been reported to reduce the corrosion resistance of the alloy through sensitization to intergranular corrosion [15].

Typical values for yield strength, tensile strength and elongation are summarized in Table 2.1 [15]. The AlMgSi alloys can contain up to 1.5% each of Mg and Si. The Mg to Si relationship is adjusted to approximately 1.73:1 in stoichiometric relationship to form the Mg_2Si intermetallic phase. The maximum solubility of this phase in aluminium is 1.85% [17]. It is also reported that the best combination of mechanical properties is obtained when the Si/Mg-relationship corresponds to the relationship of the Mg_5Si_6 intermetallic phase (wt%Si/wt%Mg = 1.39) [15].

AlMgSi-alloys have excellent corrosion properties in all natural and some artificial atmospherical conditions [15].

The use of AlMgSi alloys in automotive industry

In various car models, AlMgSi alloys are being used to replace steel skin and closure panels [18]. The 6xxx alloys has the same cold-formability, weldability and corrosion

Table 2.1: Summary of typical mechanical properties of AlMgSi-alloys [15].

$R_{p0.2}$	190 - 360 MPa
R_m	220 - 390 MPa
Elongation	12-17 %

resistance as the 5xxx series, but due to heat treatment, they have higher strength. In addition, parts made from the 6xxx series are not susceptible to Chernov-Lüders lines providing high surface quality. In addition to good appearance, heat treatable alloys will harden by the elevated temperature applied during the drying process of the paint on external body panels [16].

AA6063

The AA6063 alloy is a popular heat treatable AlMgSi alloy [19] where the total amount of Mg and Si does not exceed 1.5 %. This alloy is optimized to be easily extruded and nominally contains 1.1 % of the Mg_2Si phase [17]. The alloy is highly corrosion resistant and has good workability and weldability [19]. The alloy is widely used in both architectural applications and transportation such as pipe railings, furniture, appliance parts and trim, building products, automotive parts, vehicles, trucks and trailers [17].

AA6082

The AA6082 alloy is a heat treatable AlMgSi alloy that is suitable for high strength building and structural components [20]. The alloy is a popular alloy, especially in Europe where AA6082 has been used to replace AA6061 in many applications because of its higher strength and excellent corrosion resistance. The increase in strength is due to high amounts of Mn added [21].

The alloy has good weldability, brazeability, corrosion resistance, formability and machinability. In addition to these characteristics, its light weight and excellent mechanical properties in T6-condition has made the alloy popular in automotive, aviation and high-speed rail applications [20].

2.3 Artificial Age Hardening

The strength and hardness of heat treatable aluminium alloys can be increased by a controlled heat treatment process referred to as artificial age hardening or precipitation hardening. Natural aging can also occur at room temperature, but the time for the alloy to reach a stable condition is too long for practical applications and in industrial applications, artificial aging are commonly used.

Precipitation hardening is a heat treatment which is carried out in several steps to obtain desired phase transformations, small and evenly distributed precipitates. The main disadvantage is that the alloys will be sensitive for high temperatures and if the temperature is high enough, the precipitates will start to grow and eventually dissolve resulting in a loss in strength [8].

Precipitation hardening is suitable for alloys which have two specific characteristics displayed by the systems phase diagrams: One of the components has to have an appreciable amount of maximum solubility in the other component and the solubility limit should rapidly decrease in concentration when the temperature is decreased. This is illustrated in the hypothetical phase diagram in Figure 2.1 for a precipitation hardenable alloy of component A and B with composition C_0. Precipitation hardening is normally performed in three steps: solution heat treatment, quenching and precipitation heat treatment. This is illustrated in Figure 2.2 [8].

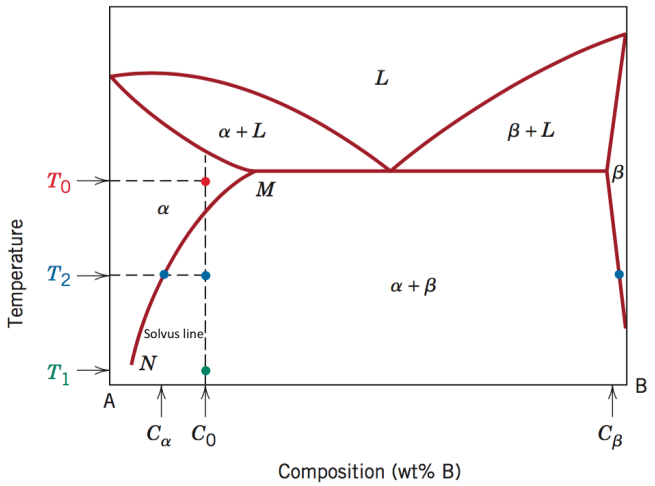

Figure 2.1: Hypotetical phase diagram for an alloy with two components, A and B, with composition C_0 [8].

Solution heat treatment

The first step of the precipitation hardening is solution heat treatment and is represented as the red line in Figure 2.2. The alloy is heated to T_0 which is over the solvus line in Figure 2.1. The alloy is kept at this temperature until all of the β-phase and other precipitates are dissolved in the α-phase. At this stage in the process, the alloy is pure α-phase with concentration C_0 of element B [8].

Quenching

Following the solution heat treatment is quenching to T_1, which normally is room temperature for metal alloys. This is performed to prevent any diffusion and precipitation of β-phase. The alloy is in a metastable condition after quenching. This means that the alloy is in a non-equilibrium state, supersaturated with B-atoms. After quenching, the alloy is relatively weak and for many alloys at T_1 this metastable condition is maintained for a long time. Some heat-treatable alloys will exhibit some natural aging as precipitates form over a long period of time [8].

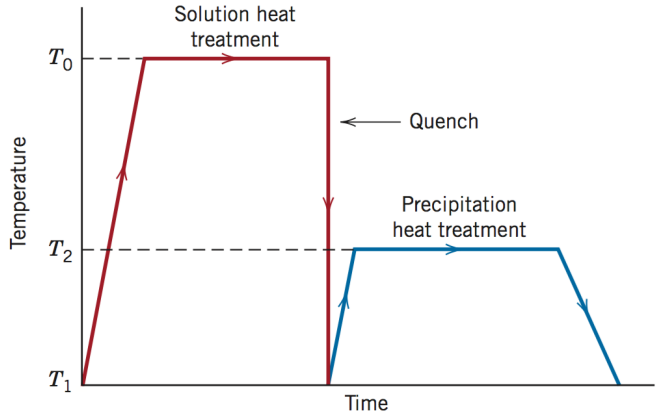

Figure 2.2: Solution and precipitation heat treatment shown schematically in a temperature-versus time plot [8].

Precipitation heat treatment

To complete the hardening process, the temperature is raised to T_2, represented as the blue line in Figure 2.2. The metastable α-phase is heated to the $\alpha + \beta$-region in Figure 2.1. This is done to increase the diffusion rate sufficiently to let β-phase precipitate as finely dispersed particles of composition C_β. T_2 is maintained until the desired amount of precipitates is obtained and then cooled to room temperature. The properties of the hardened alloy is dependent on the precipitation temperature, T_2, and the aging time at this temperature. A typical precipitation hardenable alloy will behave as shown schematically in Figure 2.3. The strength or hardness increases with time to a maximum and this reaches a maximum where the alloy is at its peak strength or hardness. The time to achieve peak hardness is dependent on alloy, time and temperature. If the temperature is maintained beyond this maximum, the strength or hardness is reduced, this is known as overaging [8].

2.3.1 Artificial Age Hardening of AlMgSi Alloys

AlMgSi alloys are characterized as heat treatable alloys and high strength can be achieved through precipitation hardening. The α-phase is a solid solution of Mg and Si in aluminium and the intermetallic compound Mg_2Si is designated as the β-phase. During the precipitation heat treatment, several transition phases are formed, designated as β''- and β'-phase. The character of these particles governs the mechanical properties. The precipitation sequence of AlMgSi-alloys is as follows [8, 15]:

$$SSSS \rightarrow GP1 \rightarrow \beta'' \rightarrow \beta' \rightarrow \beta(Mg_2Si)$$

Maximum strength coincides with the formation of a mixture of the partly coherent β'' and β' particles. Further precipitation leads to over aging, which corresponds to particle

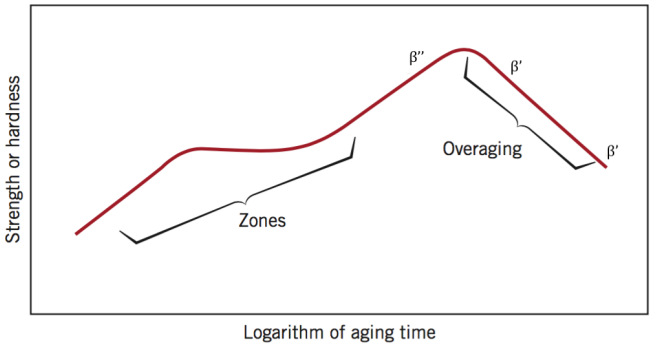

Figure 2.3: Strength or hardness as a function of time for a typical precipitation hardenable alloy. Reproduced from Callister et.al.[8].

growth and the precipitation of incoherent β particles. This associated with a reduction in strength [8, 15].

Temper Designations

Temper designations are added to the alloying number of heat treatable aluminium alloys. Each designation is a letter possibly followed by an (up to) three digit number which indicates the mechanical and/or heat treatment that the alloy has been subjected to. F, H, O and T indicates as-fabricated, strain hardened, annealed and solution heat treated, respectively [8]. In Table 2.2, common and relevant temper designations is summarized.

Table 2.2: Overview of solution heat treatment temper designations for heat treatable aluminium alloys [22, 23, 24].

Designation	Description
T1	Cooled from an elevated temperature shaping process and naturally aged to a substantially stable condition
T6x	Solution heat treated and artificially aged to under aged temper
T6	Solution heat treated then artificially aged to peak aged temper

2.4 Joining of Aluminium and Steel

Among the different alloys relevant for dissimilar metal joining, aluminium and steel alloys are the most significant materials in terms of application in the industry to enable more sustainable products. The increasing use of light-weight materials due to increasing demands in fuel efficiency standards and emissions has resulted in improvement of existing and development of new welding technologies.

Aluminium is easily joined to most metals by the use of adhesive bonding or mechanical fastening. However, special welding methods have to be applied to weld aluminium to steel. When steel is directly arc welded to aluminium, brittle intermetallic compounds may form. It is required to isolate the steel from the molten aluminium in order to prevent this and there exists two common methods to achieve this, i.e., (i) bimetallic transition inserts and (ii) coating of the steel prior to welding to improve wetting angle [1].

A prefabricated metallurgical bonded joint of aluminium and steel can be used to join aluminium to steel for structural applications [1]. Bimetallic transition inserts aren´t practically relevant for automotive application [25], but is widely used in shipbuilding, for fixing of deck houses or aluminium anodes to the steel hull. It is also used for tubing in heat exchangers and for aluminium-steel pipelines [1].

More relevant for automotive application is a coating of steel prior to welding. The steel is coated with aluminium by hot dip aluminizing or with zinc by hot dip galvanization. Once coated, the steel member can be arc welded to the aluminium member due to improved wettability [1].

The main issue associated with the joining of dissimilar metals are the local reduction in strength in the bonding area. The major challenges with the joining of aluminium and steel are connected to the large differences in mechanical and physical properties. The electrochemical potential difference, precipitates, different lattice transformation, nearly zero solid solubility and different thermal properties such as thermal expansion, heat capacity, thermal conductivity and melting point (660 °C for Al and 1497 °C for steel) makes this joint configuration specifically difficult. Several welding techniques have been applied to join aluminium and steel and the most promising are fusion- and solid-state welding. The common objective in the development or improvement of the different techniques has been to control the size and quantity of intermetallic compounds (IMC) [26].

Fe_xAl_y-phases in Welded Aluminium-Steel Joints

Intermetallic Fe_xAl_y-phases are a necessity to achieve connection between steel and aluminium. However, excessive formation of particularly Al-rich Fe_xAl_y-phases may result in brittle joints [27]. It is reported that an IMC layer thickness of 5 - 10 μm is acceptable in order to maintain good mechanical strength [28].

$FeAl$, $FeAl_2$, $FeAl_3$ and Fe_2Al_5 are the possible IMC that can form during joining of aluminium and steel as shown in Figure 2.4 and these IMC can deteriorate the mechanical properties of the joint if the IMC layer is of sufficient thickness [29]. Fusion welding techniques have been modified and improved to control the thickness of the IMC layer forming on the interface between the aluminium filler material and steel base material.

2.5 Welding

Welding is a fabrication technique where two or more metal parts are joined by application of sufficient heat so that the base materials, often in combination with a filler material, is melted. Both similar and dissimilar metals may be joined. Upon solidification, the base materials and the filler material forms a fusion zone. In the fusion zone, metallurgical bonding is achieved involving some diffusion. Adjacent to the fusion zone, there will

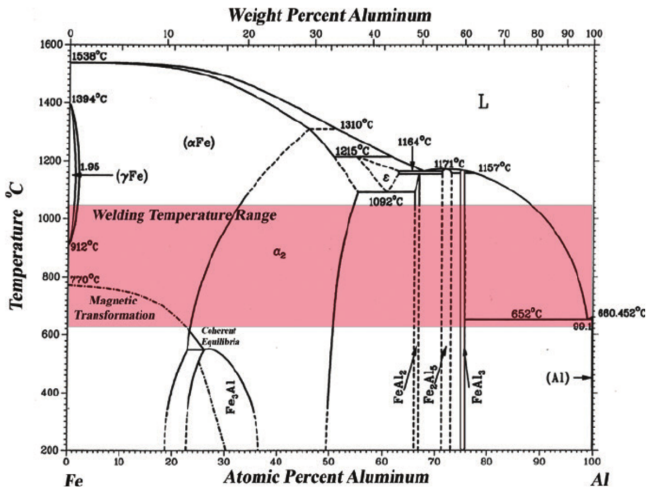

Figure 2.4: Al-Fe phase diagram showing which IMC can be formed during welding. The temperature range of welding is illustrated as the red area [29].

be a zone where the base material hasn´t melted, but the heat has affected the microstructure and properties of the base material. This zone is termed as the Heat Affected Zone (HAZ) [8].

Theoretically, the metallurgical bonding in the fusion zone can be achieved by bringing the surface atoms of each member in such close distance, in the same order as their own crystal lattice, so that the atoms form intermetallic bonds with each other. This would require chemically clean and a state of polish which is not practically possible. To overcome this impossibility, the surfaces have to be activated to eliminate foreign bodies and elements that will obstruct the formation of a bond. The most effective way to activate the surfaces is fusion, which forms metallurgical bonds by solidification and simultaneously ensures cleaning of the surfaces [30].

There are a variety of welding methods available for metal joining and further presented theory will focus on fusion welding and solid-state welding.

2.5.1 Fusion Welding

Fusion welding is the most common joining method for metals. A high-intensity heat source (e.g. electric arc, laser or electron beam) is used to provide sufficient local temperature so that the filler material and base materials are joined together by coalescence. The melting of the metals forms a fusion zone with an as-cast microstructure and a heat affected zone (HAZ) in the base material where the microstructure has been altered due to the heat input [7].

Conventional structural steels don´t exhibit softening from the microstructural changes that occur during welding. However, For aluminium the response to welding is different. The mechanical properties of the base material in the HAZ are degraded due to the mi-

crostructural changes that occur when exposed to the temperatures of fusion welding. If not welded properly, the fusion zone will have low cracking and corrosion resistance and the HAZ of heat-treatable aluminium alloys will suffer from softening. The mechanical properties of this zone will be the limiting factor and determine the mechanical strength of the joined component. The softening is due to coarsening and dissolution of the hardening precipitates. This occurs typically in the temperature range of 300 to 500 °C and may lead to a reduction in local yield strength of the HAZ up to as much as 50 %. Fusion welding is still the most used joining method for aluminium in the absence of a solid-state joining method which provides the same flexibility, productivity, robustness and cost efficiency as conventional gas metal arc welding (GMAW) or gas tungsten arc welding (GTAW) [7, 31].

Electric arc welding, such as GMAW and GTAW, is the most common process for fusion welding [5]. High heat input and no use of flux give small chances of slag entrapment in the weld. Also, the shielding gas protects the arc and causes little loss of alloying elements [26]. These methods are suitable for joining of "easier" dissimilar metals, such as carbon steel to stainless steel. The main challenge with fusion welding of dissimilar metals is the high heat input. This creates large heat affected zones (HAZ) where brittle IMC form [5].

This heat input can be calculated based on welding parameters and this is shown in Equation 2.1, where Q is heat input in kJ/mm, k is the thermal efficiency, U is the arc voltage in V, I is the welding current in A and v is the travel speed in mm/s. This equation is reproduced from the European standard EN 1011-1:2009 [32]. The thermal efficiency coefficient for MIG welding is given as 0.8.

$$Q = k\frac{U \cdot I}{v} \cdot 10^{-3} \qquad in\ kJ/mm \tag{2.1}$$

Cold Metal Transfer (CMT)

In typical GMAW, also known as MIG welding, the consumable filler material wire is continuously fed towards the base material by the use of a wire feeder. In CMT, a second motor is installed to retract the wire after the droplet reaches the weld pool as shown in Figure 2.5 [33].

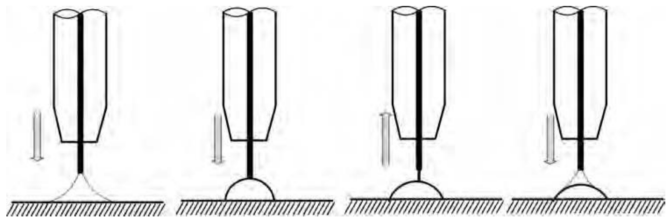

Figure 2.5: A schematic presentation of the steps in the CMT process [33].

CMT was developed to give higher precision control of the heat input and thus the thickness of the IMC layer. The CMT process is a modified MIG process which is based on a short-circuiting transfer process developed by Fronius. A wire feed system and high-speed digital control provide controlled material deposition with a low heat input. The

wire is first fed towards the weld pool creating an arc. When the electrode wire tip makes contact with the molten pool, the wire is retracted to promote the formation of a droplet that transfers to the weld pool [34]. This provides that the transfer of metal to the workpiece happens in cold condition [35]. At the same time the arc is extinguished and the current drops to near-zero, avoiding spatter. The arc is then re-ignited to start the cycle all over again [34]. By doing so, the arcing time is shortened and thus a higher precision control of the heat-input is achieved [12].

The welding parameters used in CMT-welding are crucial for the formation of IMC layers on the interface between the aluminium and the steel. As shown by Aune et.al. [29], the thickness of the IMC layer increases with increasing heat input. Madhavan et.al. [28] also showed that the heat input has an effect on the IMC-layer thickness, but when the thickness is within the 10 μm the weakest point in the weld will be the HAZ of the aluminium side because of grain growth and dissolution of strengthening particles. Thus, the heat input has to be optimized for both minimal IMC layer thickness and optimal microstructure in HAZ to increase joint strength. In addition, the wire feed rate is also affecting the heat input and thus the HAZ. An increase in feed rate will increase the heat input which will lead to a greater loss of strength in the HAZ of the aluminium [28].

2.5.2 Solid-State Welding

In manufacturing, plastic deformation is utilized most commonly in forming processes to shape mechanical parts and control their mechanical properties. However, plastic deformation can also be utilized to achieve joining without external heat input [36].

All processes where metallic bonding occurs without the presence of re-solidified liquid metal is termed as solid-state welding. Joining is achieved by applied strain and/or heat and there has to be intimate intermetallic contact between the metals without protective films and contaminations [37].

By the use of solid-state welding, parts with sufficient ductility can be joined without the use of excessive heating compared to fusion welding. Metallurgical bonding between the dissimilar metals is possible due to large plastic deformation and the breaking up of oxide layers [5].

There are several advantages with solid-state welding compared to fusion welding. By the use of solid-state welding, the microstructure of the fusion zone with its as-cast microstructure is eliminated and replaced by a thermomechanically affected zone (TMAZ) with both superior ductility and toughness. Still, with most solid-state techniques, HAZ-softening is a problem due to the reversion of hardening particles when the temperature in the HAZ is over a certain temperature. To avoid HAZ-softening the joining should be performed at temperatures below 250 °C [38].

Hybrid Metal Extrusion and Bonding (HYB)

The HYB method has been developed for solid-state joining of aluminium without HAZ-softening. An aluminium filler material is fed into a spindle extruder where it is forced to flow against an abutment blocking the wire. The pressure builds up and forces the filler wire through a die opening. The aluminium wire is continuously extruded into the groove between the two plates of the base material to be joined as shown in Figure

2.6a. The extruder head is clamped onto the base material plates which is separated to form a groove slightly smaller than the width of the extrusion die opening. The spindle extruder moves along the groove at a constant speed during the joining process and continuously extrudes filler material into the groove. The groove is completely filled with aluminium filler material and the resulting shear deformation that forms against the walls removes surface oxide layers and provides full metallic bonding. A picture of the process setup is shown in Figure 2.6b, it should be noted that this picture is not from this present project. A successful cold joining of an AlMgSi-alloy at T6 temper has been performed with HYB, resulting in no HAZ-softening [31, 38] and HYB has also recently been used to join aluminium and steel.

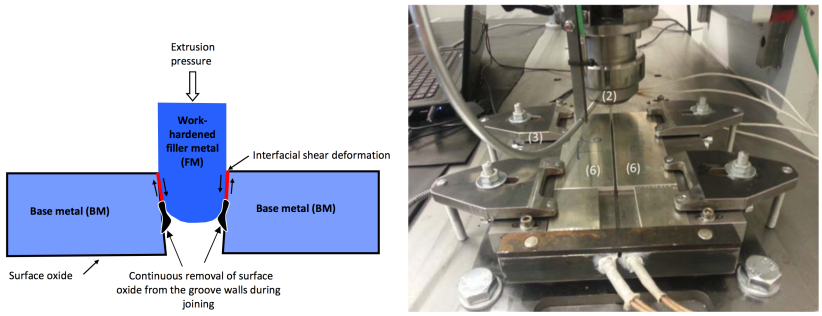

(a) Schematic representation of the HYB process.

(b) The setup of the HYB process, where the HYB spindle extruder (2), steel fixture (3) and aluminium test plates (6) are indicated.

Figure 2.6: An overview of the HYB process and setup [7].

2.6 Corrosion

Corrosion is a degradation or destruction mechanism of metals and alloys when it reacts with its environment which results in the formation of more thermodynamically stable metal-oxides, -hydroxides or -sulfides [39, 40, 41].

In this chapter, relevant corrosion mechanisms for joint aluminium and steel will be presented. The driving force for corrosion will be the potential difference of the dissimilar metals. As aluminium, which is the less noble material in the joint, is a passive material in most environments, the most relevant localized forms of corrosion attacks are also presented.

2.6.1 Galvanic Corrosion

Galvanic corrosion occurs when two metals or alloys with different practical nobility are electrically coupled. There are three essential components that need to be present for galvanic corrosion to occur; Materials with different surface potential, a common electrolyte and a common electrical path, as shown in Figure 2.7. The corrosion rate on the

least noble material will increase and the surface becomes anodic (active). The corrosion rate on the most noble material will decrease and the surface becomes cathodic [39, 42].

A simple model of a galvanic cell is shown in Figure 2.8. A net flow of current will occur from the active to the noble metal when the circuit is closed. If equilibrium conditions are assumed, a positive potential difference exists between the two metals, M and N, under open circuit conditions, as shown in Equation 2.2 [43].

$$\Delta E^{rev} = E_M^{rev} - E_N^{rev} > 0 \qquad (at\ open\ circuit) \tag{2.2}$$

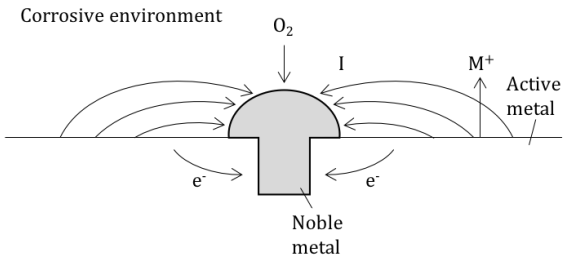

Figure 2.7: Schematic presentation of galvanic corrosion of an active metal around a noble rivet, reproduced from lecture notes on corrosion basics and engineering [43].

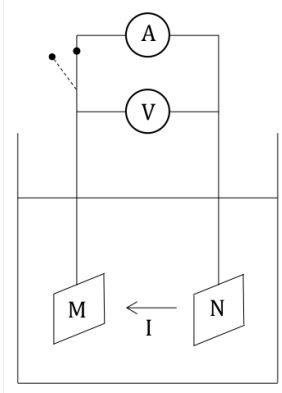

Figure 2.8: Simple galvanic cell, reproduced from lecture notes on corrosion basics and engineering [43]

.

The two metals will equilibrate at their respective corrosion potentials, $E_{corr(M)}$ and $E_{corr(N)}$, and the potential difference, ΔU, is measured by the voltmeter as shown in Equation 2.3

$$\Delta U = E_{corr(M)} - E_{corr(N)} > 0 \qquad (at\ open\ circuit) \tag{2.3}$$

When the circuit is closed, which corresponds to metallic contact between the two materials, the two metals are forced to stabilize at the same potential, as shown in Equation 2.4, as long as the ohmic potential drop is negligible. This is true if the conductivity of the electrolyte is sufficiently high. Then ΔU will be zero [43].

$$E_M = E_N = E_{couple} \qquad (at\ closed\ circuit) \tag{2.4}$$

A net positive current has to flow from N to M to maintain E_{couple}. This net current flow is maintained by an increase in oxidation of the active metal compared to open circuit conditions. The corrosion rate of the active metal increases while the corrosion rate of the noble metal decreases [43].

Metallic structures and equipment are often constructed from more than one type of metal and physical contact is often unavoidable. This makes galvanic corrosion one of the most common forms of corrosion [43]. The effect of galvanic corrosion is affected by several factors. The difference in potential between the metals and alloys will govern the electron flow and the direction. The nature of the environment, polarization behaviour of the metals and the ratio between cathodic and anodic area will govern the behaviour of the couple [42].

The galvanic series can be used to explain and predict the risk of galvanic corrosion in a given environment. The galvanic series is a good first approximation, but it has some limitations as well. Metals may form passive layers that will vary the potential over time and the open circuit potential is an expression for thermodynamic conditions that doesn't provide information about kinetics. Potential measurements are used to create practical galvanic series to display the corrosion potential of different metals in a given medium, e.g. in seawater as shown in Table 2.3 [40].

The corrosion mechanism on the anodic material(s) in the galvanic couple may take the form of general or localized corrosion. This is dependent on the configuration of the couple, the properties of the metals involved and the nature of the corrosion products that forms on the metal surface. From the galvanic series, it can be seen that aluminium is placed in the active anodic side of the series and in chloride containing solutions, aluminium alloys will be susceptible to galvanically induced localized corrosion. When localized attacks such as pitting or crevice corrosion is possible in the galvanic couple, there may be a long initiation period before the effect is observed. This has to be taken into account when conducting potential measurements. The area ratio of the cathodic and anodic surface is also a governing factor in galvanic corrosion. It is unfavourable when the surface of the cathode is large compared to the anodic member of the galvanic couple [39, 42].

Table 2.3: Summary of a practical galvanic series for metals exposed to flowing seawater with a velocity of 4 m/s and a temperature of 24 °C. Reproduced from ASM Metals Handbook [42].

Material	Steady-state electrode potential [V vs. SCE]
Carbon steel	-0.61
Cast iron	-0.61
Aluminium alloy 3003-H	-0.79
Zinc	-1.03

Galvanic corrosion is one of the major practical corrosion problems for the application of aluminium and aluminium alloys. Aluminium is thermodynamically a less noble material than most of the other metals used for construction. The passivating oxide layer, that naturally occurs on the surface and makes aluminium corrosion resistant, is easily broken down locally when the potential is increased due to galvanic coupling to a more noble material. This is particularly true in water containing chlorides or other aggressive substances [39].

The most desirable methods for investigation of galvanic corrosion in a galvanic couple is through immersion corrosion testing in the environment of interest [42]. This may be time-consuming depending on the aggressivity of the electrolyte. Galvanic corrosion is also possible in atmospheric conditions depending on the presence of elements that promote corrosion. The atmosphere is more aggressive close to the sea than in rural areas because the salinity of the moisture increases the electrical conductivity of the water [39].

2.6.2 Localized Corrosion Mechanisms

Deposit Corrosion

Deposit corrosion is a localized corrosion attack occurring under deposits where the metal surface is exposed to an electrolyte and the electrolyte is kept stagnant by the deposit. These deposits can be corrosion products, dirt, sand or marine growth [39]. This corrosion mechanism is relevant as car components are exposed to sand, dirt, dust and humidity from the road. This will deposit on the surface of exposed components and is often referred to as "road mud". Based on the nature of the humidity, this road mud can be highly corrosive.

This corrosion mechanism is a variant of crevice corrosion. Initially, the metal under the deposit corrodes by the same rate as the rest of the metal. As the metal corrodes, oxygen under the deposit is consumed and the formation of OH^- will stop. Corrosion of the metal continues and the concentration of M^+ increases under the deposit. In the absence of OH^-, Cl^- migrate into the crevice or to the corroding surface under the deposit to maintain the equilibrium in electric charge. Dissociated metal chloride reacts with water and hydrolyzes to form metal hydroxide and hydrochloric acid as shown in Equation 2.5 [39].

$$M^+Cl^- + H_2O \rightarrow MOH + H^+Cl^- \tag{2.5}$$

Hydrochloric acid will acidify the environment under the deposit. When the pH is decreased, the metal is going from a passive to active state and the passive layer will be dissolved. The corrosion rate is increasing and the process is regarded as auto-catalytic. This means that as corrosion rate increases, the migration of Cl^- also increases and subsequently, the pH is decreasing at a faster rate. As pH decreases, hydrogen reduction may supplement the cathodic reaction, further increasing the corrosion rate. The pH inside the crevice or under the deposit can be as low as pH 0-4, dependent of the combination of material and environment.

Pitting Corrosion

Pitting is a localized corrosion mechanism that can occur on passivated metals and alloys which is exposed to a medium containing ions of chlorine, bromide, iodine and perchlorate. Pitting corrosion occurs when the potential is increased beyond a critical value, E_{pit}. This value is dependent on several parameters [39].

The corrosion mechanism is characterized by narrow pits on the surface. The mechanism is similar as previously described for crevice/deposit corrosion. For completely passivated metals, such as aluminium. The mechanism is divided into two steps, initiation and growth. The theoretical foundation for initiation is not as developed as for growth. A suggested theory is that halogen ions are adsorbed into the passive layer at irregularities such as grain boundaries or inclusions. The halogen ions are increasing the conductivity of the passive layer causing local metal dissolution [39].

When aluminium is exposed to a chloride-containing electrolyte, some pitting will occur. However, if the potential is increased, e.g. when coupled to a more noble material, heavy pitting attacks can occur. Anodic dissolution will take place inside the pit as shown in Equation 2.6. The cathode reaction takes place on effective cathodes on the outside of the pit as shown in Equation 2.7 [39].

$$Al = Al^{3+} + 3e^{-} \tag{2.6}$$

$$O_2 + 2H_20 + 4e^{-} = 4OH^{-} \tag{2.7}$$

To maintain equilibrium of electric charge, chloride ions migrate into the pit. Aluminium chloride may form and hydrolyze, this will create hydrochloric acid that will acidify the environment inside the pit. The reduction of hydrogen will act as an additional cathode reaction inside the pit further increasing the corrosion rate. As aluminium is dissolved, aluminium ions diffuse out of the pit and precipitate as $Al(OH)_3$ on the surface around and on top of the pit. This will further increase corrosion rate as it traps the aggressive electrolyte inside the pit [39].

Intergranular Corrosion

Intergranular corrosion (IGC) is a localized corrosion mechanism. The corrosion attack is localized on or close to the grain boundary with relatively little visible attacks on the surface. This mechanism is particularly dangerous as the corrosion weakens the bonding between the grains. The disbonding reduces the materials toughness and sudden brittle fracture can occur at stresses lower than the yield strength [39].

The reason for IGC is that microgalvanic elements forms due to differences in concentration of alloying elements between the material at the grain boundaries compared to the rest of the material. Precipitates can cause depletion of corrosion resistant elements near the grain boundaries, such as Cr in stainless steel. Intermetallic phases, e.g. $AlFe$ or $CuAl_2$ in aluminium, may precipitate at grain boundaries forming microgalvanic elements acting either as anode or cathode. Unfavourable relationship between the area of the anode and the cathode can cause high corrosion rates [39].

Intergranular Corrosion of AlMgSi Alloys

AlMgSi-alloys where the Mg- and Si-content are balanced to form the desired Mg_2Si-precipitates, aren't particularly susceptible to IGC but excess Si increases the susceptibility [39]. However, unfavourable alloying and thermomechanical treatment may introduce susceptibility to IGC. In addition to excess Si, an increase in Cu-content above 0.1 wt% will increase the susceptibility to IGC [44].

It is also suggested that heat treatment affect IGC resistance of AlMgSi-alloys. IGC susceptibility of AlMgSi alloys is dependent on quenching rate after solution heat treatment and degree of artificial aging [44, 45, 46]. IGC susceptibility is introduced if the alloy is slowly quenched after solution heat treatment. The IGC resistance further decreases during artificial aging and is lowest at peak hardness, T6. If overaged, the IGC resistance increases again [44]. However, Svenningsen et. al. [45] reported that IGC susceptibility is high in naturally aged condition for an AlMgSi alloy with small copper content (0.13 wt%). Artificial aging to peak hardness eliminates susceptibility to IGC while over-aging introduces susceptibility to pitting corrosion. The results from this study are presented in Figure 2.9. The elimination of IGC susceptibility is attributed to the coarsening and discontinuation of a copper-rich grain boundary film during artificial aging. Pitting susceptibility in over-aged condition were attributed to the coarsening of cathodic Q-phase ($Al_5Cu_2Mg_8Si_6$) particles internally in the body of the grains.

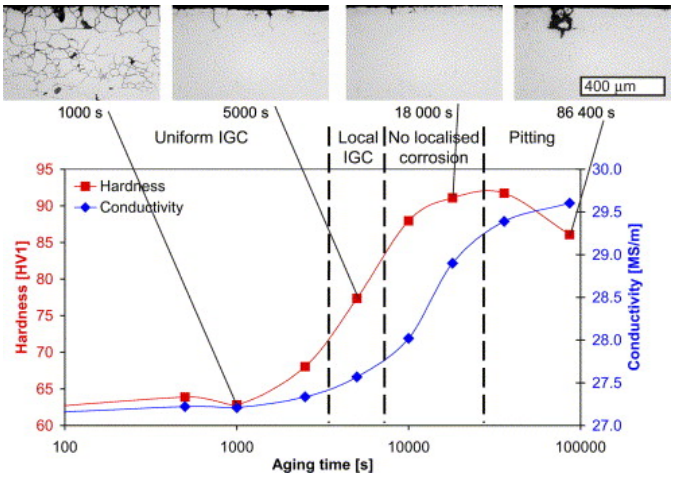

Figure 2.9: Corrosion susceptibility as a function of artificial aging time at 185 °C aging temperature [45].

2.6.3 Corrosion of Welded Aluminium-Steel Joints

The interest in joining of aluminium and steel is growing in the automotive industry due to the demands for lighter more fuel-efficient vehicles. However, most studies aim to improve mechanical property of the joints and studies that focus on the corrosion behaviour of such joints are rarely reported [6]. Joining of aluminium and steel by welding exclude the possibility to avoid galvanic coupling. However, the corrosion resistance is

dependent of several parameters. The filler material, formation of IMCs and a galvanic zinc layer may have an influence on the corrosion resistance of the weld [47].

Wloka et.al.[47] performed salt spray tests and microelectrochemical measurements of laser beam joints of AA6016 to galvanized steel using two different filler materials, ZnAl2 and AlMg6Mn. The weld material was found to be most prone to corrosion and the corrosion rate was governed by the connection to effective cathodes such as steel. The connection between the aluminium base material and filler material was not accelerating the corrosion. The results also showed that the formation of IMCs should be avoided as the IMC also behave as effective cathodes. During joining, the Zn-coating on the galvanized steel improves the wetting behaviour of the brazed seam between the filler material and the steel base material. The Zn is melted during welding and a Zn enriched zone is formed at the runout of the weld seam. Although zinc improves wetting and is essential to produce a joint with fusion welding, the zinc was reported to lower the corrosion resistance and the reliability of the weld. In contact with a corrosive environment, zinc is the first element to corrode due to low nobility. The zinc-rich zone was found to leave a crevice between the filler material and the steel which is highly prone to further corrosion.

LeBozec et.al.[48] performed accelerated corrosion tests in accordance with N-VDA. N-VDA is a newly accelerated corrosion test developed by the German association of automotive industry (VDA) in collaboration with the German steel association (VDEh). The test was developed to replace VDA 621-415 which has been shown to exaggerate the corrosion of Zn-coatings and thus does not simulate relevant road conditions. The joints in this study were not welded, but joined by adhesives and clinching. The test was performed on 20 different material configurations, but in essence, the materials used were carbon steel, high strength steel, galvanized steel and the aluminium alloys AA5182 and AA6061. The various joints were rated based on thickness measurements and loss of mechanical properties. The loss of mechanical properties was related to corrosion degradation in the overlapping area that induced a modification of failure mode.

Shi et.al.[6] conducted a study on laser welding, FSW and CMT using an immersion corrosion test in a solution known as EXCO solution. This was compared to corrosion potential measurements. The study showed that galvanic corrosion did occur and that the corrosion rate was increasing with increasing heat input during welding. The IMC layer leads to a dissolution of the adjacent filler material and it is suggested that the IMC layer thickness should be precisely controlled to maintain good corrosion resistance. This study tested two different filler materials and the AlMg filler material was found to be superior to the AlSi filler material in terms of corrosion. In addition, Zn enriched areas were found to decrease the corrosion resistance of welded joints. This further confirms the findings from Wloka et.al.[47].

2.6.4 Scanning Kelvin Probe

The Scanning Kelvin Probe (SKP) technique is a unique reference electrode [49] and a non-destructive test method used to study fundamental processes of corrosion [50]. SKP belongs to a group of scanning microscopy techniques including Scanning tunneling microscopy, atomic force microscopy/Scanning Kelvin Probe Force Microscopy (SKPFM), conductive atomic force microscopy and scanning capacitance microscopy. These techniques use sharp needles that scan over the sample extremely close (from nm to μm) to

the surface. The spatial resolution of SKP is on the micro level usually in the range of 50 - 250 μm. [51]. The drawback of the SKP technique is that it requires considerable efforts for reliable operation.

The SKP technique measures the potential difference that is generated between two metals that are in electrical contact, but separated by a small gap. The reason for the potential difference is that conductive metals have electrons distributed on different energy levels, known as Fermi levels. When electrically coupled, the Fermi levels will be equalized and electrons will start flowing. The work it requires to move these electrons is indicated by the work function. The difference in electric potential outside each metal induces the appearance of an electrostatic field in the gap between them. The potential of this field is the contact potential difference and corresponds to the difference in work function (or electrochemical potential) of the two materials [51]. In SKP one of the metals will be the sample that is electrically connected through the sample table to a needle, typically made from a Ni-Cr alloy. The instrument is typically calibrated above a $Cu/CuSO_4$ saturated electrode and this enables the possibility to convert and refer to the surface potential with respect to the desired reference potential, e.g. SHE or SCE [50].

SKP can be used to measure the potential changes on bare metal surfaces [52] and this potential can be translated to the corrosion potential. It is possible to obtain precise information on the distribution of areas that are anodic and cathodic and this can be used to rank surfaces by their ability to reduce oxygen and thus, their tendency to corrode. With SKP, it is possible to measure potential versus time at a single point, make a line scan or trace a potential map over an area of a sample [50]. The ability to measure and map the potential of a surface with a lateral resolution of around 100 μm is useful, especially in studies of localized corrosion of aluminium alloys [53].

Chapter 3

Experimental procedure

3.1 Materials

Two different AlMgSi alloys in two different temper conditions were studied in this work. The aluminium alloys were welded to a dual phase steel and exposed to accelerated corrosion testing. The chemical composition of each alloy are given in Table 3.1 and 3.2. The process history of the aluminium alloys received from Hydro is provided in Appendix B.

A galvanized dual phase (DP) steel, HCT600, was delivered as 1.5 mm thick plates by Benteler Automotive with a Z140 zinc coating, meaning that there is 140 $g\ zinc/m2$ which corresponds to a 10 μm coating thickness. Two extruded plates of the 6xxx-series, AA6063 and AA6082, 3 mm thick aluminium plates in T1 temper condition were delivered from Hydro Sunndalsøra, the chemical composition of the aluminium alloys are given in Table 3.1. The plates were cut into smaller sections and heat treated to two different temper conditions, T6x (under aged) and T6 (peak aged). These were welded by CMT to the steel plates by the use of a solid wire for gas shielded metal arc welding with a chemical composition within the limits for the alloy symbol Al 4043A (AlSi5) given in Table 3.3 which is in accordance with ISO 18273, standard for welding consumables [54]. The composition of the steel base material is given in Table 3.2, which is obtained from EN10346:2015 [55], standard for metal coated multiphase steels.

Table 3.1: Chemical composition of the aluminium base materials and filler materials, given in wt%.

Alloy	Fe	Si	Mg	Mn	Cr	Cu	Zn	Ti	Ga	V
AA6063	0.184	0.520	0.646	0.012	0.001	0.020	0.006	0.011	0.011	0.005
AA6082	0.220	1.000	0.810	0.530	0.140	0.100	0.005	0.010	0.010	-

Table 3.2: Chemical composition of the steel base material, given in wt%.

Alloy	C	Si	Mn	Al	Cr + Mo	Nb + Ti	Coating
HCT600	0.18	0.80	2.20	0.015 - 2.0	1.0	0.15	Z140*

*Zinc layer thickness $\sim 10\mu m$

Table 3.3: Chemical composition of the filler materials, given in wt%.

Alloy	Fe	Si	Mg	Mn	Cr	Cu	Zn	Zr	Ti	B
AlSi5 (CMT)	0.6	4.5-6.0	0.2	0.15	-	0.30	0.10	0.15	-	-
AA6082-T4 (HYB)	0.20	1.11	0.61	0.51	0.14	0.002	-	0.13	0.043	0.006

3.2 Precipitation Hardening

The heat treatment of the aluminium alloys was performed in Nabertherm N30/85HA, air circulation furnace. The heat treatment was carried out in two steps, solution- and precipitation heat treatment which is presented graphically in Figure 3.1.

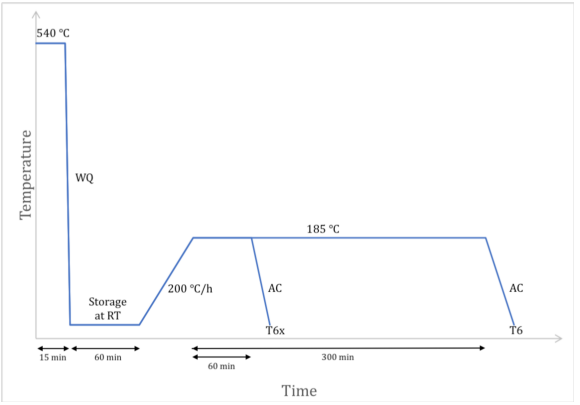

Figure 3.1: Schematical overview of the thermal history for used for both AlMgSi-alloys to obtain T6x and T6 condition, respectively. WC = Water quenched, AC = Air cooled, RT = Room temperature. Made by the author.

1. **Solution heat treatment:** All of the plates were placed into the furnace after it had reached 540 $°C$. The plates were put into the furnace and solution heat treated for 15 minutes followed by quenching in water. The plates were kept at room temperature for one hour to allow some natural aging. Then the plates were put into a freezer to stop the natural aging.

2. **Precipitation heat treatment:** When the furnace reached room temperature, the samples were taken from the freezer and placed into the furnace and heated to 185 $°C$ with a heating rate of 200 $°C/h$. The plates were kept at this temperature for 1 and 5 hours to obtain T6x- and T6 temper condition:

- **T6x:** To obtain the under aged temper, the plates were heated to 185 $°C$ and kept for 1 hour, followed by air cooling to room temperature.

- **T6:** To obtain the peak aged temper, the plates were heated to 185 $°C$ and kept for 5 hours, followed by air cooling to room temperature.

Hardness was measured in every step of the precipitation hardening process starting with the as-received condition followed by SHT-, T6x- and T6 condition. In addition, images of the microstructure were captured in the as-received condition and after SHT.

3.3 Welding

3.3.1 CMT

The aluminium plates were cut to match the as received dimensions of the steel plates at 370x110 mm. The plates were welded in a lap joint configuration with the aluminium plate on top of the steel plate with approximately 10 mm overlap. From every weld sample, eight slices with a width of 40 mm were prepared for metallographic examination, tensile testing and corrosion testing. An overview of this is shown in Figure 3.2.

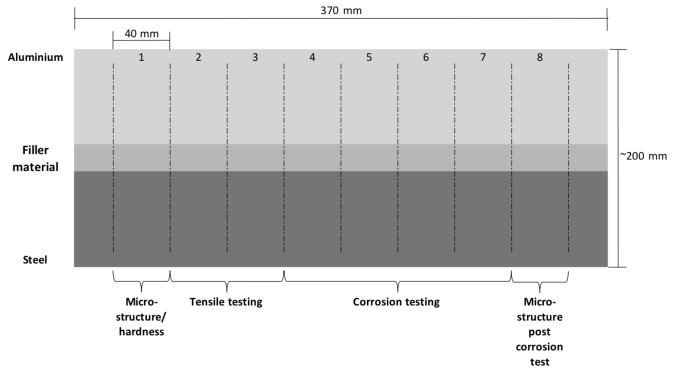

Figure 3.2: Overview of welded samples and how they were cut and prepared for further testing.

Four combinations of alloy and temper conditions were welded by CMT and two aluminium plates were to be welded by HYB, a summary of material and welding method combinations are presented in Table 3.4.

Table 3.4: Combinations of materials, pre treatments and welding methods

Test	Lower material	Pre treatment	Upper material	Filler material	Welding method
1	HCT600	$10\mu m$ Zinc	AA6063-T6x	AlSi5	CMT
2	HCT600	$10\mu m$ Zinc	AA6063-T6	AlSi5	CMT
3	HCT600	$10\mu m$ Zinc	AA6082-T6x	AlSi5	CMT
4	HCT600	$10\mu m$ Zinc	AA6082-T6	AlSi5	CMT
5	HCT600	$10\mu m$ Zinc	AA6063-T6	AA6082-T4	HYB
6	HCT600	$10\mu m$ Zinc	AA6082-T6	AA6082-T4	HYB

The CMT welding was performed with Fronius TPSi 400, automated CMT welder. The steel plates were used in the as-received condition and joined to the each of the aluminium alloys in both temper conditions. A lap joint configuration was produced with the aluminium plate placed on top of the steel plate with an overlap of 10 mm and the plates were fastened and aligned by steel rivets prior to welding. The rivets were later removed when samples were prepared from the weld. The filler wire was aimed perpendicular to the sample with 0 mm offset with respect to the edge of the aluminium plate for all of the CMT weld specimens and pure argon was used as shielding gas. The welding parameters were kept constant but some small variations were observed in the output from the machine post welding. Welding parameters are presented in table 3.5. The post welding parameters were not recorded for weld 3 and 4, but it was confirmed by the operator that these parameters were similar to weld 1 and 2. The real values could then be used to calculate the resulting heat input. This was calculated to be between 0.115 - 0.120 kJ/mm for all welds by the use of equation 2.1.

Table 3.5: Welding parameters of CMT welded plates.

		Pre set			Measured post welding		
Test	**Welding speed [mm/s]**	**Current [A]**	**Voltage [V]**	**Wire feeding [m/min]**	**Current [A]**	**Voltage [V]**	**Wire feeding [m/min]**
1	9	85	12.9	5.7	94	13.8	6.4
2	9	85	12.9	5.7	94	14.4	6.4
3	9	85	12.9	5.7	-	-	-
4	9	85	12.9	5.7	-	-	-

3.3.2 HYB

The setup of the HYB welding method is initially made for butt welding. In a feasibility study performed by Hybond AS in conjunction with this master thesis, it was concluded that new tool development was required to produce lap joint identical to the joints made by CMT and this was not possible in the time frame of this project. However, for this project Hybond was able to modify their equipment to produce a lap joint to match the samples welded by CMT based on the idea of plug welding. This was done by milling of a slot in the upper material where the aluminium filler material was extruded into the slot by the

rotating pin. This technique was inspired by plug welding, but due to the geometry of the milled groove, this method is further referred to as HYB slot welding. A 3D model of the setup was produced by Hybond and is presented in Figure 3.3. The zinc coating on the steel was removed by grinding as bare metal surfaces are desired in HYB joining.

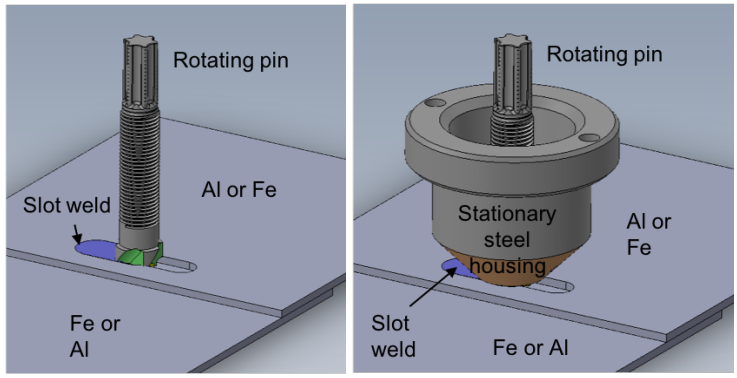

(a) Pin-in-groove situation **(b)** Steel housing in place

Figure 3.3: Model showing the setup of the slot welding method where no new tool developments were required, reprinted by permission from HyBond AS [56].

3.4 Material Characterization in LOM

The microstructure of the base materials and welded samples were examined by the use of a light optical microscope (LOM). Images of the base materials were used to compare the microstructure in the as-received condition with the microstructure after SHT and welding.

3.4.1 Sample preparation

Cross-sectional samples of each weld specimen were cut with Struers Discotom, water-cooled cutter. The samples were then cold-mounted in EpoFix and ground to plane by the use of Struers RotoPol-31 with water as lubricant and waterproof SiC grinding papers ranging from p320 - p1200. The samples were then polished by the use of Struers Tegramin-30 with 9, 3 and 1 μm diamond suspensions with the corresponding polishing discs.

To reveal the microstructure of the aluminium-steel welded samples in LOM, different etching methods were applied. The aluminium samples were anodized in 5 % HBF_4 for 90 s by the use of Struers Lectro-Pol, electropolisher. To prevent dissolution of the steel during anodizing, the steel was coated with conventional nail polish. This was applied by hand with the included brush and allowed to dry completely before exposure to the solution. A picture of the coated sample, prepared for anodizing, is shown in Figure 3.4. The coating was removed by acetone before examination in the microscope. The steel

samples were chemically etched in 2 % Nital for 10-15 seconds, it was not necessary with any coating on the aluminium during this etching.

Figure 3.4: Nail polish was used to coat the steel side of the weld to prevent dissolution of steel during anodizing.

3.4.2 LOM imaging

Images of the microstructure were captured with LEICA MEF4M, optical microscope with Jenoptik Laser Optik System camera and a suitable objective. The objectives that were used ranged from 2.5x to 100x, depending on the microstructure of the investigated alloy. The microstructure of all samples was examined parallel to the extrusion direction, as shown schematically in Figure 3.5

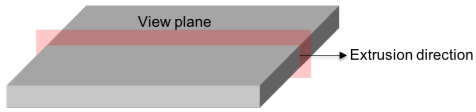

Figure 3.5: Schematic presentation of the view plane in imaging of the microstructure of both base materials and welded samples, made by the author.

For the samples where the aluminium was anodized, images were captured in by the use of a crossed polarizer/analyzer and a sub-parallel λ-plate. Images of the etched steel samples were captured with the microscope set to bright field mode. Also, ground and polished samples were used to examine the weld and its effect on the zinc-coating by the use of bright field mode.

The images were captured by the use of ProgRes Capture v.2.8.8, imaging software connected to the camera in the microscope. To create an overview of the microstructural zones in the welded samples, micrographs captured with the 2.5x objective were stitched together using image editing software, Pixelmator v.3.7.

3.5 Hardness measurements

Vickers hardness was measured by the use of Zwick/Roell ZHV30, automatic hardness tester. The load and dwell time was set to 1kg (HV1) and 10 s, respectively, for hardness

indents in both the aluminium and steel side of the samples. The hardness of the base material was measured by five parallels on the surface of the sample as shown in Figure 3.6. For the aluminium plates hardness was measured before heat treatment and in the SHT-, T6x- and T6 condition. Hardness distribution over the welded samples was measured by three series, respectively one at the top (I), middle (II) and bottom (III) of the weld, as shown in Figure 3.7.

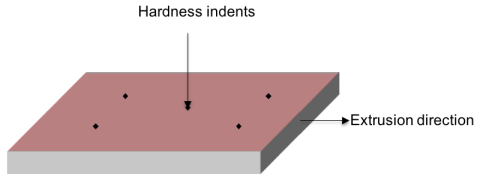

Figure 3.6: Schematic presentation of the surface where the hardness was measured on the base materials, made by the author.

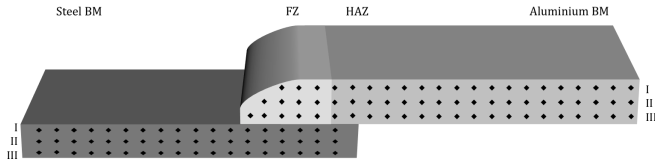

Figure 3.7: Schematic presentation of how the hardness profiles were measured. The indentations were divided into three series, top (I), middle (II) and bottom (III). FZ = Fusion Zone, HAZ = Heat Affected Zone, BM = Base Material, made by the author.

3.6 Accelerated Corrosion Testing

Five samples of each weld were exposed to corrosion testing to determine the effect of alloy, temper condition and welding method on the corrosion resistance. The open circuit potential (OCP) was logged during the corrosion test by the use of a Gamry potentiostat with a saturated KCl reference electrode (SCE) and Gamry Instruments Framework, computer software. This setup could have been made easier by the use of a multimeter with the possibility for data logging, but due to availability, the potentiostat was used in this project.

By logging the OCP, the time for the zinc coating to completely corrode away could be monitored. A test run of the experiment was conducted to determine the time intervals between each sample collection. As can be seen in Figure 3.8, the initial potential was -1025 mV for the first 6-7 hours, then the OCP increased to -730 mV and was stable for the rest of the test. This increase in OCP indicates that the zinc has completely corroded away and that whats left is bare steel and aluminium.

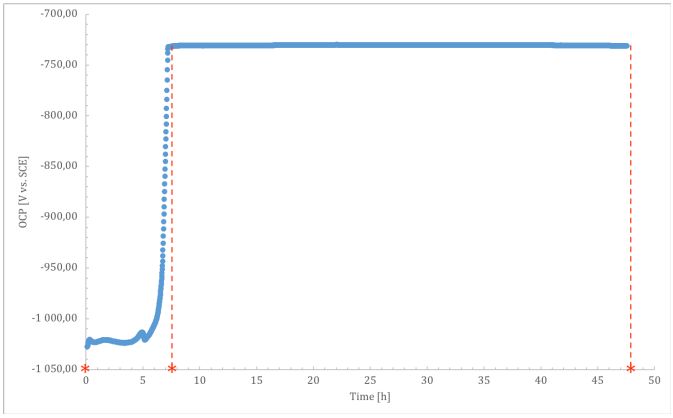

Figure 3.8: OCP monitored during the test run of the experiment. The red star indicates the intervals that was decided for tensile testing.

Based on this test run, it was decided to collect two samples after the OCP indicated that the zinc coating had corroded away. The remaining three samples were collected after 48 hours in the test solution and two of these were used for tensile testing and one was used to characterize the corrosion attacks in LOM. These results were compared to the tensile test results of samples that weren't exposed in the corrosion test.

3.6.1 Sample preparation

Before corrosion testing, the samples were machined to tensile test specimens by the use of a water jet cutter. A threaded hole was machined at the aluminium side of the weld to enable cable connection with the potentiostat. This was done by personnel on NTNUs workshop. The samples were degreased in acetone before exposure in the test solution. One sample from each weld was connected to the potentiostat by a cable that was fastened by a screw to one of the five exposed samples. The cable connection were then coated with bee wax to isolate from the test solution to ensure that the connection didn't disturb the test results. A picture of a prepared sample with cable connection is shown in Figure

3.6.2 Test solution

The test solution was prepared based on the salt solution used in ASTM G85 [57]. 5 $\pm$ 1 wt% of NaCl was dissolved in distilled water and the pH was adjusted to 2.8-3.0 by addition of 10 ml of glacial acetic acid per litre solution. The test was performed at room temperature, measured to 25 °C.

3.6.3 Test setup

The samples were placed in four beakers with a volume of 5 liters. Each alloy and temper condition were separated into separate beakers. One of the samples that were prepared with a cable connection and coating was connected with the potentiostat for logging

of OCP. The rest of the samples that were prepared with a cable connection were used for momentarily checks of the OCP by the use of a separate multimeter and reference electrode, this reference electrode was of the same type and model SCE as used for the continuous logging of OCP. This was done to check that the condition in each beaker was the same as in the one where the potential was logged before the samples could be collected. A picture of the test setup is shown in Figure 3.9.

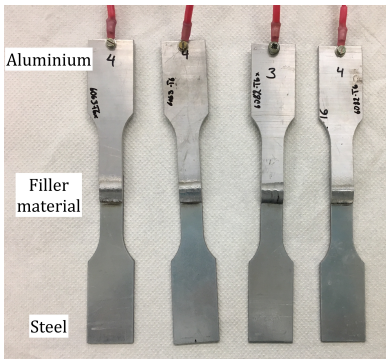

(a) Uncoated samples

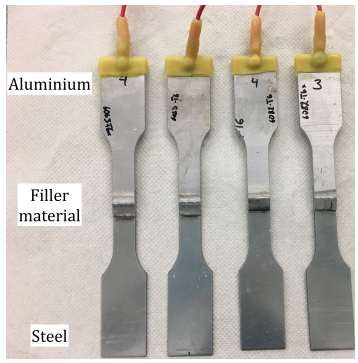

(b) Coated samples with bee wax

(c) Samples in separate beakers

Figure 3.9: Corrosion test setup

3.6.4 Tensile testing

Two samples of each weld were tensile tested before corrosion testing, two samples were tensile tested after approximately 7 hours when the zinc coating was completely corroded away. Finally, two samples were tensile tested after 48 hours exposure in the test solution. This was done to investigate the strength loss due to corrosion as a function of

time. A single lap shear tensile test was performed to quantify the strength loss due to corrosion. The dimensions that were used for the tensile test specimens are presented in Figure 3.10. The tensile test was performed on w+b Series LFV 100 kN, servohydraulic universal testing machine in accordance with ISO 6892, standard for tensile testing of metallic materials.

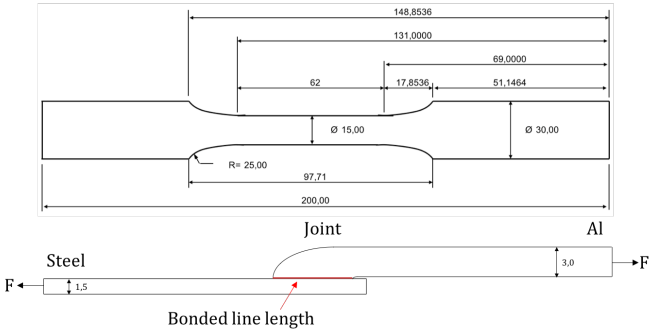

Figure 3.10: Dimensions of the tensile test specimens given in mm.

3.6.5 Characterization of corrosion mechanism in LOM

In addition to tensile testing, one of the samples that had been exposed in the corrosion test for 48 hours were prepared for characterization of corrosion attacks. A cross-section of the corroded weld was produced of the weld nugget and 10 mm each side were cut and mounted in EpoFix epoxy resin, ground to plain and polished by the same procedure as previously described. The samples were examined in LOM without any etching or anodizing.

3.7 Energy Dispersive Spectroscopy analysis

Energy Dispersive Spectroscopy (EDS) analysis has been used to identify the mix of elements in the fusion zone. After corrosion testing, the areas of interest were analyzed in EDS by the use of Hitachi SU-6600, FESEM. This analysis where performed on two uncorroded samples of the CMT weld, AA6082-T6 and AA6063-T6. The samples were ground and polished as previously described, down to 1 μm diamond suspension. After cleaning in ultrasonic bath and ethanol the samples were dried and put into sample bags together with pouches of silica gel to absorb any moisture.

During the EDS analysis, the accelerating voltage and working distance were set to 15 keV and 15 mm, respectively. The accelerating voltage was adjusted based on that Al, Fe and Zn were the elements of interest. The working distance is the recommended distance for optimal detection of the x-ray signals emitted from the sample during EDS analysis.

3.8 Scanning Kelvin Probe analysis

The Scanning Kelvin Probe (SKP) has been used to measure the surface potential in the fusion zone of one of the welds. Several scanning methods were used, including point scans, line scan and surface scans. Potential measurements were carried out with a commercial height-regulated SKP from Wicinski-Wicinski. The probe was a needle made of NiCr (80/20) with a tip diameter of 170 μm. The potential of the probe was calibrated against a $Cu/CuSO_4$ electrode in humid air at $\sim$95 % relative humidity. The working distance for all measurements was set to 50 μm and all the potentials are given relative to a standard hydrogen electrode (SHE). The humidity in the chamber was kept constant at the desired level by the use of an automated control system.

A sample was embedded in epoxy and ground to plane as previously described. In SKP analysis, the sample surface should be as fresh as possible when the analysis starts. This is due to the building up of oxides on the metal surfaces. The sample was polished down to 1 μm by tge same procedure as previously described, rinsed in ethanol and dried before the sample were put in a sample bag together with silica gel pouches to absorb any moisture left on the sample. The sample was brought directly to the SKP machine and preparations were commenced. Liquid nitrogen was used to separate the sample from the epoxy.

An image of the sample table and the instrument chamber is shown in Figure 3.11. The sample was placed on the sample table and electrically connected to the sample table by the use of a conducting glue containing silver. The sample is slightly rotated because the instrument is only able to perform scans along the x-axis of the sample table. A small copper beaker was also glued to the sample table by the use of the same conducting glue. The beaker was filled with a saturated $CuSO_4$ solution that is used as a $Cu/CuSO_4$ reference electrode with a known potential of +320 mV vs. SHE. This was later used to calibrate the instrument.

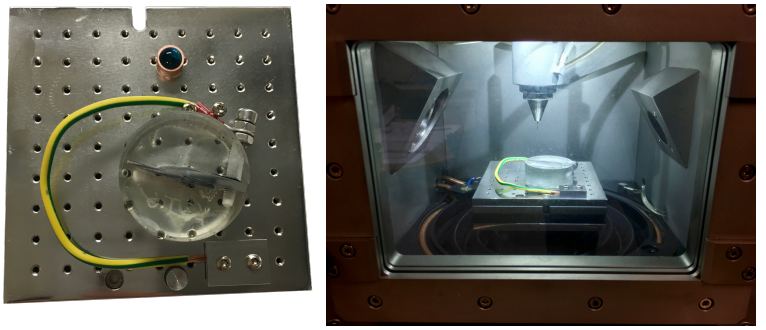

(a) SKP sample table **(b)** Instrument chamber

Figure 3.11: Setup of the SKP experiment. It should be noted that in the final experiment the sample was not embedded in epoxy as shown in this image. The epoxy was removed to ensure electric connection to the instrument.

The sample table was placed into the chamber and the climate was regulated to 25

$°C$ and 95 % relative humidity (RH). The sample was left in the chamber for 1.5 hours to allow equilibrium conditions to stabilize before the test could be commenced. After 1.5 hours, the SKP signal was cleaned to compensate for electromagnetic noise that may originate from the motors of the instrument and also the surroundings this reduced the error to 9 mV. It is desired that the error of the signal should be between 2.5 - 8 mV. A NiCr-needle was used with a diameter of 170 μm, this defines the resolution of the SKP-signal.

A test program was programmed into the computer software to perform several scans of the surface potential as shown in Figure 3.12. For the line and surface scans the steps between each measurement was set to 50 and 100 μm, respectively. A summary of the scans is presented in Table 3.6. This program was set to repeat itself over a time period of 24 hours.

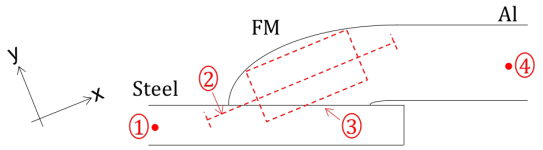

Figure 3.12: Overview of the different SKP scans that were conducted on the sample surface. The coordinate system shows the sample orientation on the sample table.

Table 3.6: Program for SKP scans repeated over a period of 24 hours.

Scan	Type	Comment
1	Point scan	Surface potential of steel base material
2	Line scan	Surface potential across the interface
3	Surface scan	Surface potential mapping of an area of 2x3 mm
4	Point scan	Surface potential of the aluminium base material

Chapter 4

Results

4.1 Precipitation Hardening

Both of the aluminium alloys, AA6063 and AA6082, were precipitation hardened to T6x and T6 condition. The microstructure of AA6063 consisted of equiaxed grains with an increasing grain size towards both surfaces. After solution heat treatment (SHT), grain growth was identified as shown in Figure 4.1.

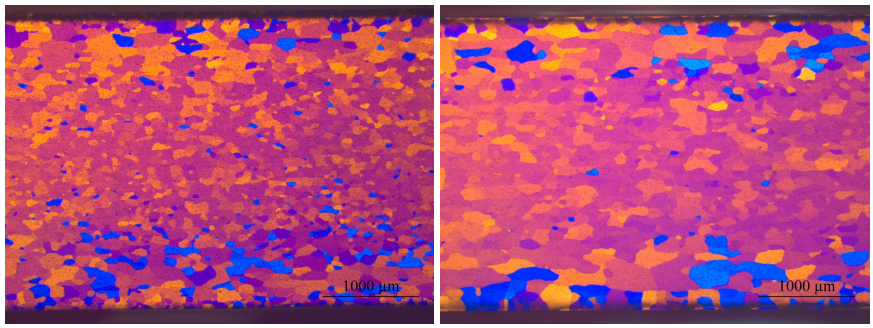

(a) T1, as received condition. **(b)** SHT

Figure 4.1: Microstructure before and after Solution Heat Treatment (SHT) of AA6063.

The microstructure of AA6082 was a fibrous, as shown in Figure 4.2a, with a recrystallized layer at the top and bottom of approximately 110 μm. After solution heat treatment (SHT) the fibrous structure and the thickness of the recrystallized layer was still maintained, but the recrystallized layer was subjected to grain growth as shown in Figure 4.2b.

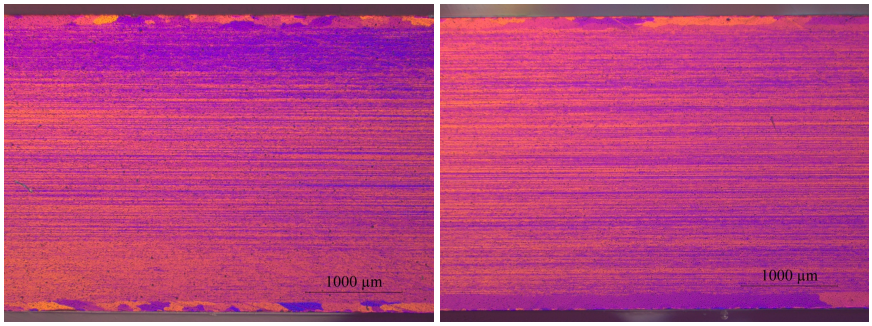

(a) T1, as received condition. **(b)** SHT

Figure 4.2: Microstructure before and after solution heat treatment (SHT) of AA6082.

Vickers hardness was measured before, during and after the precipitation hardening process and the results are given in Figure 4.3, where the hardness evolution of both aluminium alloys are presented together with the temperature profiles used to achieve the T6x and T6 temper conditions. There was a decrease in hardness for both alloys when solution heat treated. When artificially aged the hardness increased above the as received T1 condition for both alloys.

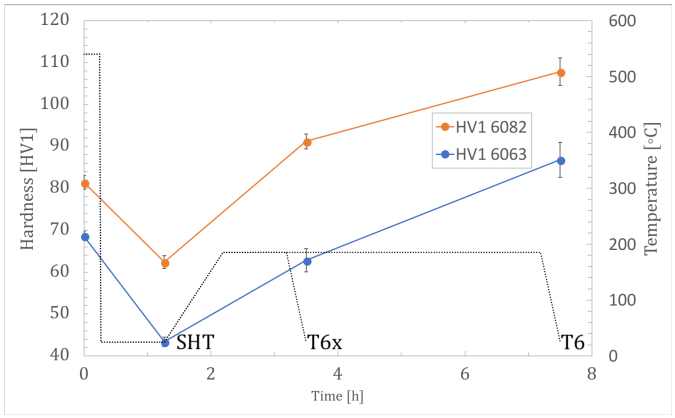

Figure 4.3: Hardness evolution of the aluminium alloys, AA6063 (blue) and AA6082 (orange), during precipitation hardening including standard deviation. The temperature profiles for the two temper conditions is shown as dotted lines. SHT = Solution heat treated.

The AA6063 is the softest of the aluminium alloys with a hardness of 63 HV1 in under aged condition. In peak aged condition the hardness increased to 87 HV1. The hardness of AA6082 in under aged condition was 91 and in peak aged condition the hardness increased to 108 HV1. The hardness of the dual phase steel, HCT600, was 211 HV1. The Vickers hardness measurements are summarized in Table B.1 in Appendix B.

4.2 Welding

All of the material combinations were more or less successfully welded by CMT. A picture of weld specimen number four is shown in Figure 4.4. Some trouble was experienced with the welding of specimen number three. The first trial had to be discarded and re-welded due to the formation of large dimples in the filler material. New plates of the same materials were welded again and the result was still not perfect, but due to a limited number of plates available, the weld had to be kept for further testing.

(a) Weld

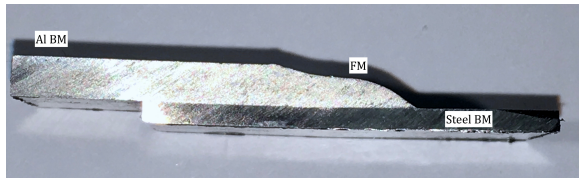

(b) Cross section

Figure 4.4: 6082-T6 joined by CMT to HCT600-Z140 by the use of an AlSi5 FM. FM = Filler material, BM=Base Material.

Plates of the same materials were also delivered to HyBond for test trials of the slot welding method. HYB slot welding trials were successful as shown in figure 4.5. However, the required amount of samples for corrosion testing couldn't be produced within the time window of this project due to material shortage.

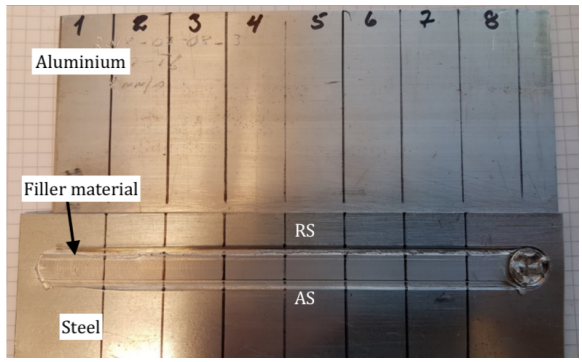

(a) Weld

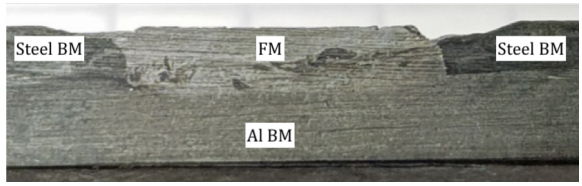

(b) Cross section of weld

Figure 4.5: 6082-T6 joined by HYB slot welding to HCT600-Z140 by the use of a 6082-T4 Al FM. BM=Base Material, FM=Filler Material, RS=Retreating Side, AS=Advancing Side. Results presented with permission from HyBond AS[58].

Four different welding trials followed by tensile testing were performed by HyBond with the HYB slot welding method. Testing of the HYB weld was not performed by the author, but results are presented with permission from HyBond AS[58]. Images of the tensile test specimens are given in Figure 4.6 The first slot welding trial resulted in insufficient groove filling and the tensile specimen broke at 140 N. By reducing the welding speed from 8 to 6 mm/s, three samples with good groove filling were produced. Tensile tests revealed that two samples that fractured in the grip hole in the aluminium side at 6072 N and 6504 N for series 2 and 4, respectively. The third sample fractured within the filler material at 8368 N. This corresponds to a tensile strength of 310 MPa which is close to tensile tests of the filler material measured by SINTEF in earlier work.

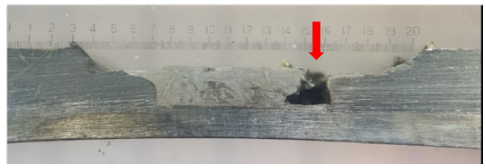

(a) Series 1,

(b) Series 2

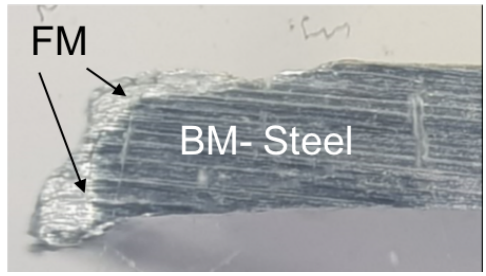

(c) Series 3

(d) Series 3

Figure 4.6: The four tensile test specimens of slot welded trials tested by HyBond. Results presented with permission from HyBond AS[58]

An overview of all the planned welding specimens for this project are shown in Table 4.1 and specimens that were included in further corrosion testing is indicated by green.

Table 4.1: Combinations of materials, pre treatments and welding methods for every welding experiment. Also the samples included in further corrosion testing is indicated by green.

Specimen	Lower material	Upper material	Welding method	
1	HCT600	AA6063-T6x	CMT	
2	HCT600	AA6063-T6	CMT	
3	HCT600	AA6082-T6x	CMT	
4	HCT600	AA6082-T6	CMT	
5	HCT600	AA6063-T6	HYB	
6	HCT600	AA6082-T6	HYB	

4.2.1 Effect of welding on hardness

The hardness distribution over each of the weld specimens was measured to determine the influence of the heat input during welding on the base materials. The hardness of the base material, HAZ and filler material

AA6063-T6x

The hardness distribution over weld specimen 1 is shown in Figure 4.7a. It can be seen that the hardness of the AA6063-T6x base material is slightly decreasing down to the hardness of the filler material in the fusion zone, but a distinctive HAZ in the base material can´t be identified. The filler material in the fusion zone has the lowest hardness at 50 HV1 which is a slight under match compared to the aluminium base material. The steel base material has a hardness of around 200 HV1 and a slight decrease in hardness down to 190 HV1 can be identified below the fusion zone of the weld.

AA6063-T6

The hardness distribution over weld specimen 2 is shown in Figure 4.7b. It can be seen that the hardness of the AA6063-T6 base material has been reduced from 87 down to 52 HV1, which corresponds to a 40 % reduction in hardness. The size of the HAZ can be measured to approximately 11 mm. The filler material in the fusion zone has the lowest hardness at 50 HV1 which is an under match compared to both the aluminium base material but the fusion zone matches the hardness of the HAZ. The steel base material has a hardness of around 200 HV1 and a slight decrease in hardness down to 190 HV1 can be identified below the fusion zone of the weld.

AA6082-T6x

The hardness distribution over weld specimen 3 is shown in Figure 4.7c. It can be seen that the hardness of the AA6082-T6x base material has been reduced from 91 down to 57 HV1, which corresponds to a 35 % reduction in hardness. The size of the HAZ can be measured to approximately 10 mm. The filler material in the fusion zone has the lowest hardness at 54 HV1 which is a significant under match compared to both the base material and its HAZ. The steel base material has a hardness of around 200 HV1 and a slight decrease in hardness down to 190 HV1 can be identified below the fusion zone of the weld.

AA6082-T6

The hardness profile over weld specimen 4 is shown in Figure 4.7d. It can be seen that the hardness of the AA6082-T6 base material has been reduced from 108 down to 63 HV1, which corresponds to a 42 % reduction in hardness. The filler material has the lowest hardness at 48 HV1 which is a significant under match compared to both the base material and its HAZ. The steel base material has a hardness of around 200 HV1 and an increased scatter in hardness values may indicate that the steel has been affected by the heat from welding.

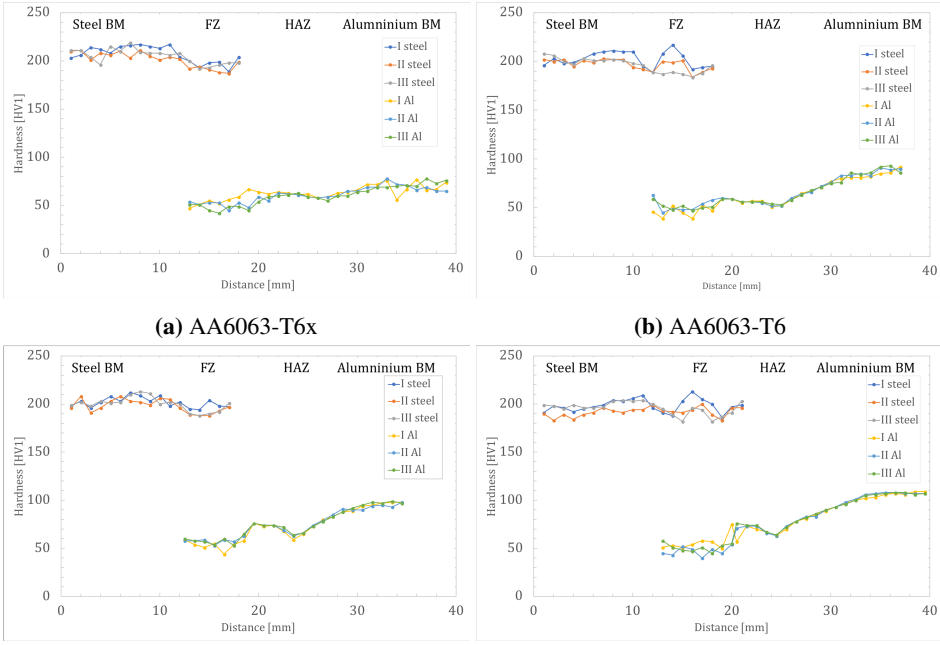

(a) AA6063-T6x

(b) AA6063-T6

(c) AA6082-T6x

(d) AA6082-T6

Figure 4.7: Hardness distribution over weld specimens where the hardness is measured in three parallels. I = top, II = middle, III = bottom, BM = base material, FZ = fusion zone, HAZ = heat affected zone.

4.2.2 Effect of welding on microstructure

AA6063

The equiaxed microstructure of the AA6063 alloy is preserved towards the fusion zone as can be seen for both T6x and T6 condition in Figure 4.8. No recrystallization or grain growth from the welding can be identified.

AA6082

The fibrous microstructure of the AA6082 alloy is maintained towards the fusion zone, except for a small area at the bottom of the fusion zone in the welded AA6082-T6 sample, as can be seen in Figure 4.9b. Here a small zone in the base material has been subjected to recrystallization and grain growth.

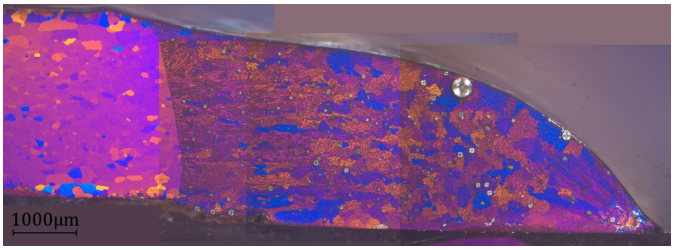

(a) AA6063-T6x

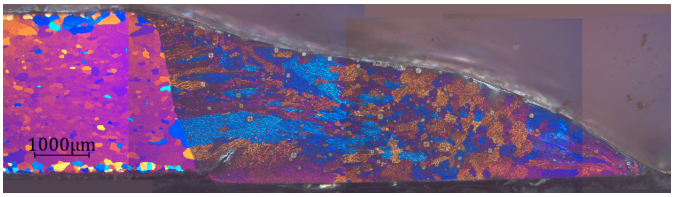

(b) AA6063-T6

Figure 4.8: Overview of microstructural zones in the aluminium side of welded AA6063 in T6x-(4.8a) and T6 condition (4.8b).

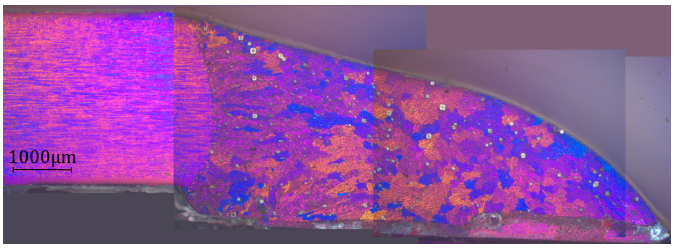

(a) AA6082-T6x

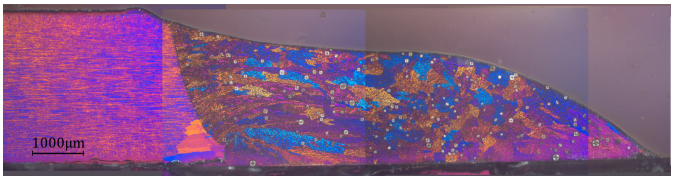

(b) AA6082-T6

Figure 4.9: Overview of the microstructural zones in the aluminium side of welded AA6082 in T6x (4.9a) and T6 condition (4.9b).

Filler material

The microstructure of the filler material is similar for all four weld samples and a micrograph of this is shown in Figure 4.10. The filler material has an as-cast microstructure with coarse grains that consists of two phases. The light continuous phase that is shown in

Figure 4.10b is evenly distributed throughout the filler material. Also, a large amount of porosity can be seen in the filler material.

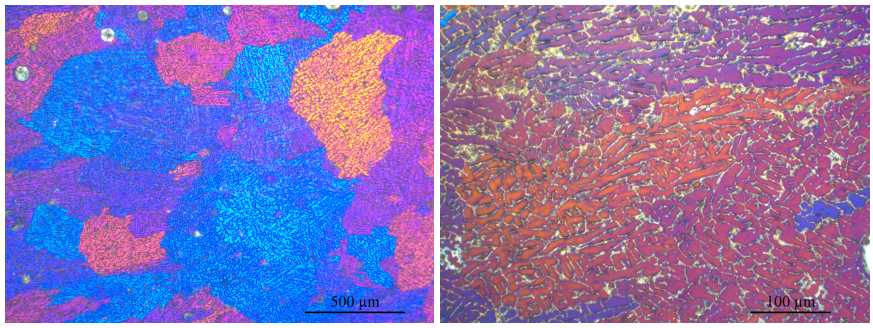

(a) **(b)**

Figure 4.10: Microstructure of the filler material, showing the aluminium matrix surrounded by continuous structure.

IMC layer

On the interface between the aluminium filler material and the steel, an IMC layer is present. The thickness of this layer is uniform across the interface in the order of 3 to 4 μm. In position 1, Figure 4.11 position 1, a crack can be seen between the IMC layer and the steel. The crack shows a lack of fusion in this particular weld.

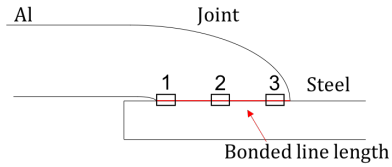

(a) Schematic overview of the position of the following micrographs of the interface between aluminium filler material and steel.

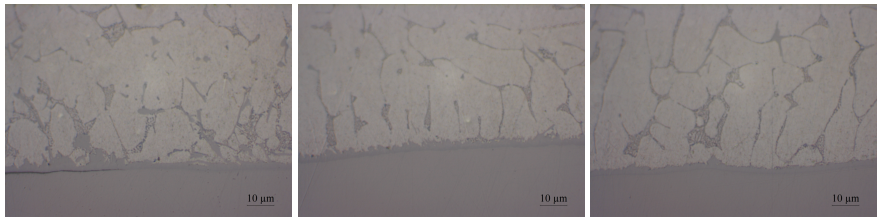

1 2 3

Figure 4.11: IMC layer at three positions on the interface between steel and aluminium.

Steel

In Figure 4.12, the microstructure of the steel below the fusion zone is compared to the microstructure of the base material in mid-thickness of the steel plate. The steel has a fine-grained microstructure consisting of ferrite (light phase) and martensite (dark phase) in both micrographs.

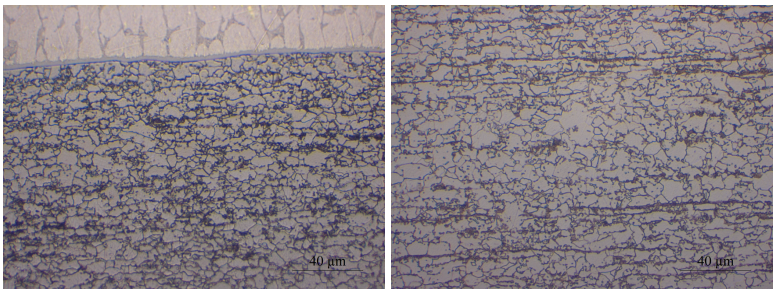

(a) Microstructure below the fusion zone **(b)** Mid thickness of the base material

Figure 4.12: Comparison of the steel microstructure below the fusion zone and the base material.

4.2.3 Effect of welding on the zinc coating

The average zinc coating thickness on the steel was measured to $9.0 \pm 2.3\ \mu m$. From the micrographs of the welded AA6082-T6 sample, it can be seen that an area close to the weld toe is left without zinc coating after welding. This is shown in Figure 4.13a. This area has a width of approximately 1000 μm and bare steel is left exposed. The zinc layer was measured as shown in Figure 4.13b. At this point, the zinc coating thickness was measured to 9.2 μm. A total of 25 measurements were performed to determine the average coating thickness.

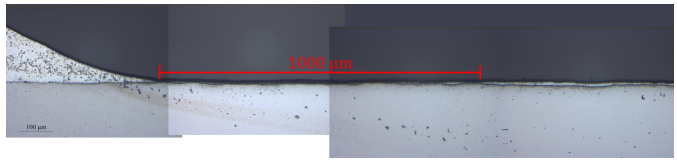

(a) Close to the weld toe, 1000 μm is left as bare, uncoated steel after welding. The scale bar in the image is 100 μm.

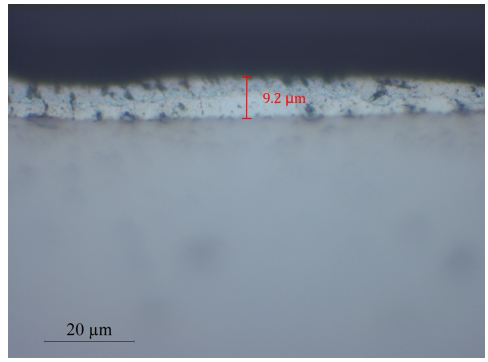

(b) The zinc coating thickness was measured far away from the weld. This shows one of the measurements where the zinc coating was measured to 9.2 μm.

Figure 4.13: The zinc that originally covered the steel has been removed close to the weld.

4.3 Accelerated Corrosion Testing

The corrosion test was carried out over a 48 hour time period and tensile testing was performed on two parallels before, during and after the test to measure the strength loss due to corrosion as a function of time. The open circuit potential was logged from one of the test beakers. The strength of the joints was compared to the fracture mode and finally, the corrosion attacks were investigated in the light optical microscope.

4.3.1 Potential evolution during corrosion test

Immediately after the samples were immersed in the corrosion test, some instabilities in the open circuit potential (OCP) was observed, but the OCP stabilized at -1040 mV vs. SCE after approximately an hour. At this point in the test, heavy gas development was observed at the zinc coated steel side of the weld. After five hours of immersion, it could be seen that the zinc coating was gradually dissolving and more bare steel was exposed. After eight hours of testing, a sudden increase in OCP occurred. In the meantime, it could be observed that no zinc was left on the steel. The gas development on the steel side diminished and two samples were collected for tensile testing. On the remaining samples gas development was observed to gradually occur on the aluminium side of the weld, the closer to the fusion zone, the heavier the gas development.

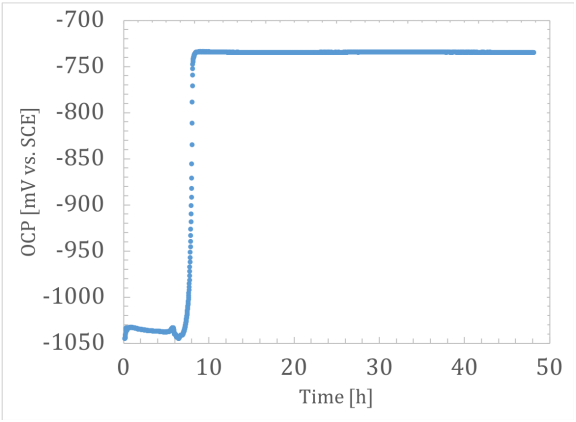

Figure 4.14: The evolution of open circuit potential (OCP) during 48 hours of corrosion testing. This curve was recorded from the test beaker that contained the AA6082-T6x sample.

4.3.2 Strength loss due to corrosion

Welded samples were tensile tested before corrosion testing. The samples failed at low deformation which is shown in the engineering stress-strain curve for the AA6082-T6 sample in Figure 4.15. This shows that the fracture occurs before any plastic deformation takes place. The stress is calculated by the use of the cross-sectional area of the aluminium plate, but due to the complexity in stresses and strains in a tensile test of such lap joints, the maximum load at failure is used for further analysis instead of yield- or tensile strength.

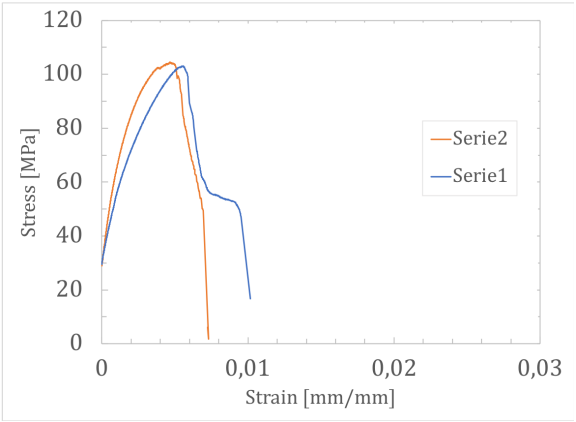

Figure 4.15: Engineering stress vs. strain curve for two samples of welded AA6082-T6 before corrosion.

For three of the four welded samples, AA6063-T6, -T6x and AA6082-T6, the fracture occurred in the interface between the aluminium filler material and base material, as can be seen in Figure 4.16a. After eight hours of immersion in the corrosion test solution, the

fracture had moved and occurred along the bonding line between the filler material and the steel plate as shown in Figure 4.16b.

The AA6082-T6x sample had a significantly lower max load than the other samples and unlike the other uncorroded samples, the fracture on this sample occurred along the bonding line.

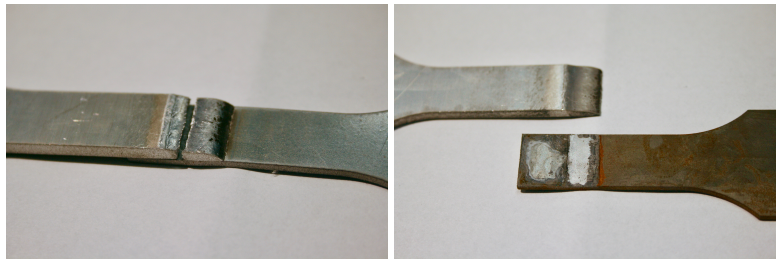

(a) Tensile test specimen prior to corrosion testing, fracture occurred on the interface between aluminium filler- and base material.

(b) Tensile test specimen after corrosion testing, fracture occurred along the bonding line between aluminium filler material and steel plate.

Figure 4.16: Comparison between fracture before (a) and after (b) corrosion testing.

AA6063-T6x

In Figure 4.18, a comparison of tensile test specimen before, during and after corrosion testing is shown. By comparing the three samples in Figure 4.17a, it can be seen that the zinc coating on top of the steel base material is removed after eight hours of exposure except for a small area where the aluminium and steel plates overlapped each other. Based on a comparison of the fracture surfaces on sample 2 and 3, it can be seen that the bonding surface area in the fusion zone appears to have been reduced by corrosion. Also after 48 hours, pitting corrosion is visible on the surface of the aluminium base material.

The fracture before corrosion testing occurred on the interface between filler- and base material at a maximum load of 4646 and 5396 N for the two series, respectively. After the first eight hours of exposure, the fracture occurred along the bonding line, this resulted in a reduction in maximum load to 2234 and 2578 N, respectively. Finally, after 48 hours of corrosion testing, the maximum load was measured to 2596 and 2450 N, respectively. The strength loss is presented graphically in Figure 4.17b.

(a) Tensile test samples.

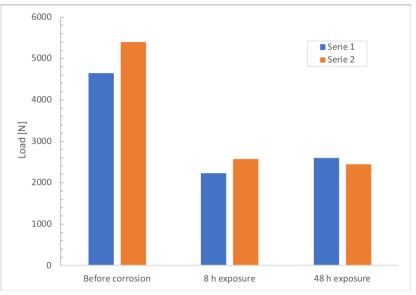

(b) Strength loss before, during and after corrosion testing.

Figure 4.17: Comparison of tensile test samples before corrosion(1), after eight hours(2) and 48 hours(3) of immersion with strength loss for the AA6063-T6x sample. BM = Base material, FZ = Fusion Zone

AA6063-T6

The same development in corrosion and fracture behaviour as for the AA6063-T6x was observed for the AA6063-T6 sample as shown in Figure 4.18a. The zinc coating was removed after eight hours of immersion, some zinc is left under the overlapping plates and the bonding surface area was reduced after 48 hours. However, no visible corrosion attacks can be identified by visual inspection.

The maximum load to fracture before corrosion was measured to 5024 and 5296 N, respectively. After eight hours of exposure, the strength was reduced to 3258 and 3613 N. Finally at end of the corrosion test, the maximum load to fracture of the joint was further reduced to 2756 and 2331 N. This is presented graphically in Figure 4.18b.

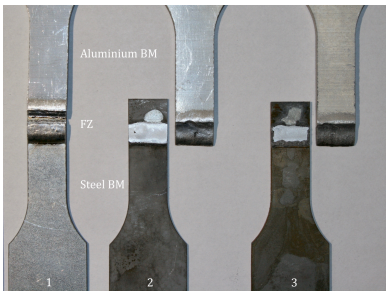

(a) Tensile samples before corrosion testing (1), after eight hours (2) and 48 hours of exposure.

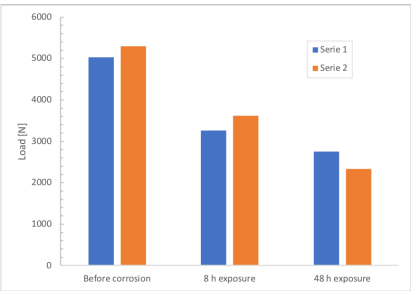

(b) Strength loss as a function of time.

Figure 4.18: Comparison of tensile test samples and strength loss for the AA6063-T6 sample.

AA6082-T6x

All of the tensile test specimens of the AA6082-T6x weld fractured along the bonding line between the filler material and the steel plate regardless of corrosion which can be seen in Figure 4.19a. The dimples in the filler material in the fusion zone occurred during welding as previously described. As for the other samples, it was observed that the zinc was completely removed after eight hours of immersion and that the bonding surface area has been reduced after 48 hours. Finally, no visible corrosion attacks can be identified by visual inspection.

As shown in Figure 4.19b, the maximum load before corrosion was measured to 3108 and 3854 N. After eight hours of immersion, the strength was reduced to 2737 and 2934 N. After 48 hours the load was 2574 and 2660 N.

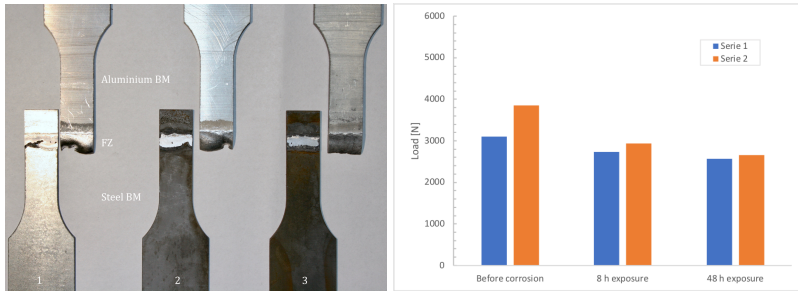

(a) Tensile samples before corrosion testing (1), after eight hours (2) and 48 hours of exposure.

(b) Strength loss as a function of time.

Figure 4.19: Comparison of tensile test samples and strength loss for the AA6082-T6x sample.

AA6082-T6

Before corrosion, the AA6082-T6 joint fractured on the interface between the filler material and aluminium base material. After both eight and 48 hours immersion, the joints fractured along the bonding line. This can be seen in Figure 4.20a. Some zinc can also be seen left under the overlap on both samples after corrosion. No visible corrosion attacks can be seen by visual inspection.

The strength loss is shown graphically in Figure 4.20b. Before corrosion, the tensile strength of the joint were 103 and 105 MPa. The strength reduced after eight hours of immersion down to 61 and 59 MPa. After 48 hours of corrosion, an increase in tensile strength can be seen for both series up to 64 and 79, respectively.

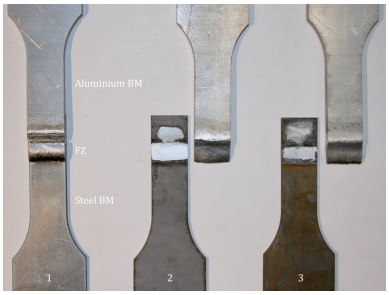

(a) Tensile samples before corrosion testing (1), after eight hours (2) and 48 hours of exposure.

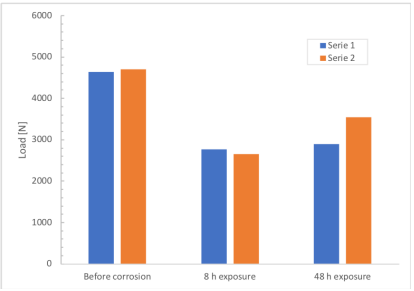

(b) Strength loss as a function of time.

Figure 4.20: Comparison of tensile test samples and strength loss for the AA6082-T6 sample.

4.3.3 Characterization of corrosion attacks

The effect of corrosion could to some extent be seen by visual inspection, but to determine the difference between the different alloys and temper condition, the corrosion attacks was investigated in the light optical microscope. The following micrographs are taken after 48 hours of immersion in the corrosion test.

AA6063-T6x

The AA6063-T6x is the sample that had visible pitting corrosion after 48 hours, as presented above. Micrographs showing the corrosion attacks on the base- and filler material of the AA6063-T6x sample is shown Figure 4.21. From the micrographs of the base materials, it can be seen that the corrosion attacks have a different appearance for the different positions. Further away from the fusion zone, the corrosion attack can be characterized as local IGC. The occurrence and depth of these local IGC attacks are decreasing, but the formation of pits is increasing closer to the fusion zone. There is an area on the interface between the base material and filler material that looks unaffected which has a width of about 2 mm. The filler material has been subjected to a uniform corrosion attack over the entire surface. Finally, the weld toe has suffered from severe corrosion attacks that has dissolved the filler material and formed large pits. The corrosion attack has propagated 3 mm along the bonding line under the filler material.

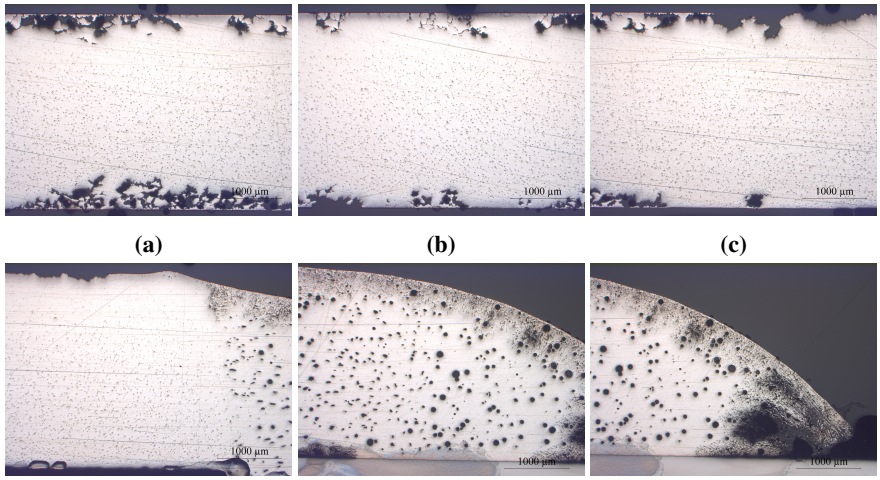

Figure 4.21: Corrosion attacks on AA6063-T6x from the base material (a) to the filler material (f).

AA6063-T6

Micrographs showing the corrosion attacks on the base- and filler material AA6063-T6 sample is presented in Figure 4.22. The base material has been subjected to uniform IGC attacks that is approximately 425 μm deep from both sides, but the attack on the base material stops about 10 mm away from the fusion zone and the area towards the filler material is unaffected of the corrosion test. The filler material has suffered from general corrosion on the entire surface. The heaviest corrosion of the filler material is the weld toe where filler material is dissolved and a 2 mm long crack has formed between the filler material and the steel plate.

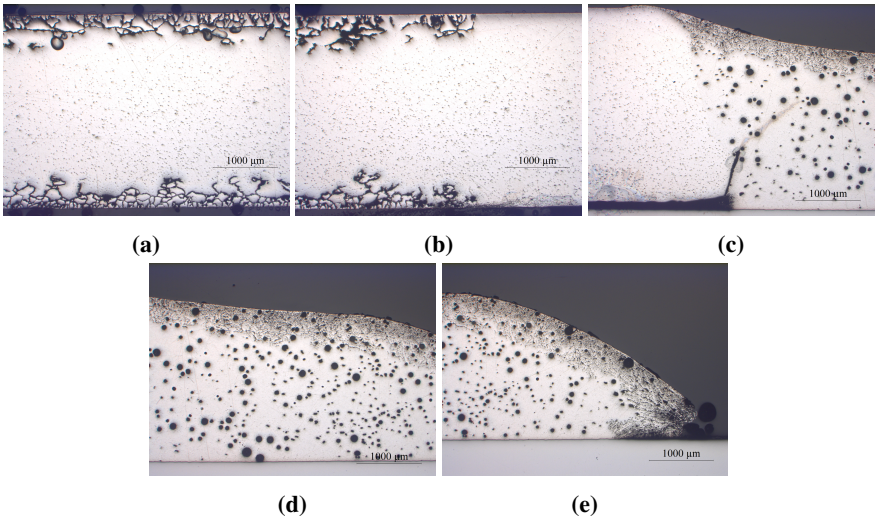

Figure 4.22: Corrosion attacks on AA6063-T6 from the base material to the filler material.

AA6082-T6x

The micrographs of corrosion attacks on the base- and filler material of the AA6082-T6x weld are presented in Figure 4.23. No corrosion was found on the base material while some corrosion can be seen on the filler material surface, but this is not as uniform and not as deep as was seen for the previous samples. However, severe corrosion can be seen in the weld toe where the filler material is dissolved. The corrosion attack doesn't propagate as a crack between the steel, but is more uniform dissolution than for the AA6063 samples.

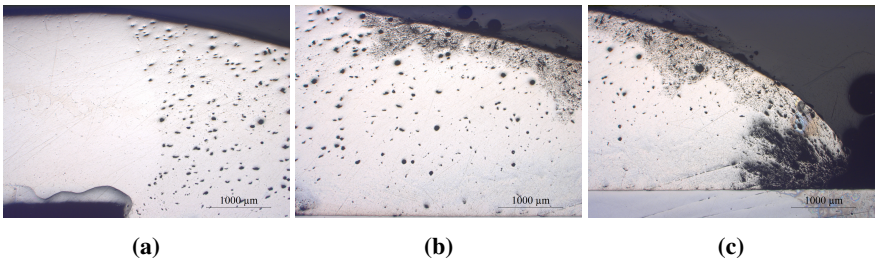

Figure 4.23: Corrosion attacks on AA6082-T6x from the base material to the filler material.

AA6082-T6

For the record, the micrographs of the corrosion attacks on the base- and filler material on the AA6082-T6 sample that is shown in Figure 4.24 is presented in opposite direction compared with the previous micrographs.

From the micrographs, it can be seen that neither the base material nor the filler material has been subjected to corrosion attacks. However, the weld toe has suffered from

severe corrosion. A large amount of the filler material has dissolved and large pits have formed between the filler material and the steel plate. A crack 2.5 mm long crack has formed due to dissolution of filler material. Some small pits were observed at random positions close to the surface in the base material.

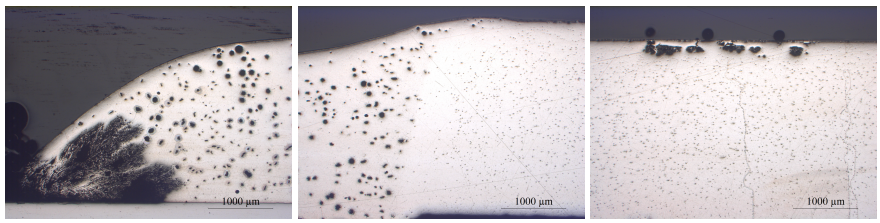

(a) **(b)** **(c)**

Figure 4.24: Corrosion attacks on AA6082-T6 from the base material to the filler material.

4.3.4 EDS analysis

The EDS analysis of the AA6082-T6 weld is shown in Figure 4.25. The area that was analyzed is shown in 4.25a. It can be seen from the backscatter electron image, that this area consists of at least three different phases based on atomic number contrast. The EDS analysis indicates that there is a mix of aluminium and zinc in the filler material. A zinc rich zone was also found close to the steel plate. Finally, no mixing of elements were observed in the steel.

In the filler material, a light and a dark phase is distinguishable in the aluminium filler material as can be seen in Figure 4.25a. A zone close to the steel plate was found to be rich in zinc. Also, a zinc-rich phase were found to surround aluminium grains in the further into the filler material.

A line scan was performed over the same interface and phases. It can be seen that the lines for wt% of aluminium and zinc is mirroring each other in the filler material. Where the line passes across the darker phase, the main constituent is aluminium. Where the line passes over the light phase, the aluminium content is reduced while the zinc content increases.

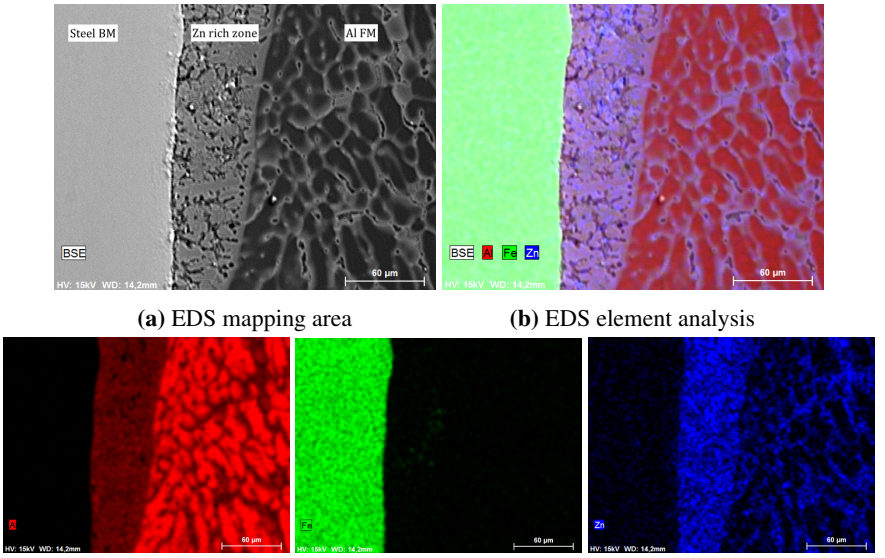

(a) EDS mapping area **(b)** EDS element analysis

(c) Al **(d)** Fe **(e)** Zn

Figure 4.25: Energy dispersive spectroscopy mapping of the interface between aluminium filler material and steel base material in the AA6082-T6 weld.

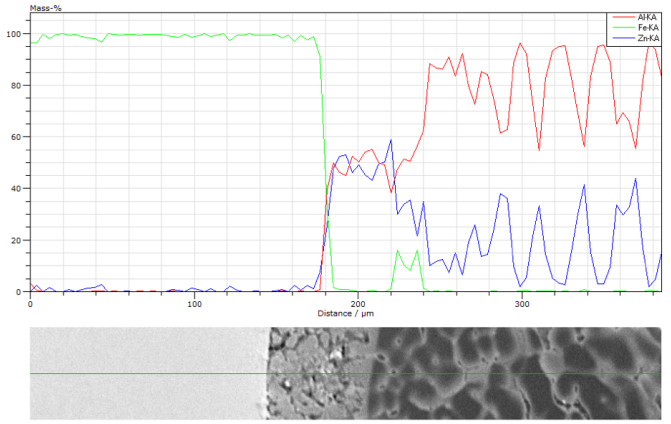

Figure 4.26: Line scan across the interface of the steel-aluminium interface.

4.3.5 Scanning Kelvin Probe (SKP) analysis

Point Scans

In Figure 4.27 the potential is plotted as a function of time. The sample was put into the test chamber at 12:42 at 95 % RH, which is defined as t=0. The first point scans started after 6 hours. The potential of steel is in the passive region and increasing from 70 mV vs.

SHE up to 150 mV vs. SHE over the course of 14 hours. For alumninium the potential is stable between -364 to -371 mV vs. SHE, but the last measurement is lost due to an unforeseen shut-down of the test program that happened before the final point scan on the aluminium side.

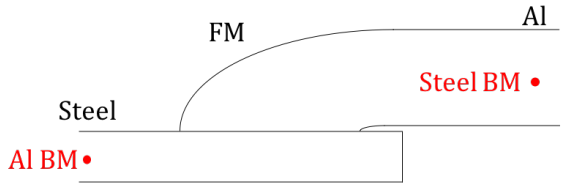

(a) Schematic representation of the position of the point scans.

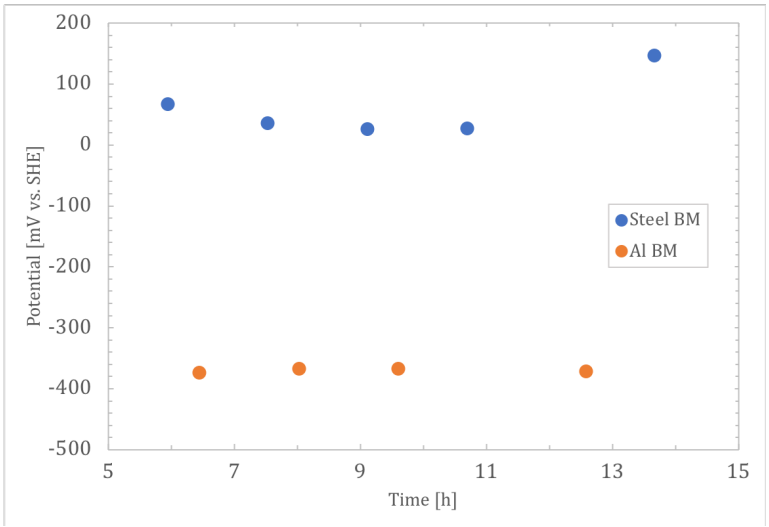

(b) Potential versus time.

Figure 4.27: Potential as a function of time for the points in the steel BM and aluminium BM, respectively. BM=Base Material.

Line Scans

The line scan was performed such that the potential measurement started above the steel base material, but very close to the surface to obtain a line scan through the tip of the filler material and further into the filler material ending up in the aluminium base material. The line scan and a schematic presentation of the position of the line is presented in Figure 4.28a. Five scans were performed, and the first was obtained after the sample had been exposed to the climate in the chamber for 6 hours, the following scans were obtained after 7.5, 9, 11 and 13.5 hours, respectively. From the scans, three potential plateaus can be distinguished. First, the steel potential at around 5 mV vs. SHE. Next, the potential of the filler material is around -100 mV vs. SHE and finally, the potential of aluminium is at

around -180 mV vs. SHE. The potential had increased along the entire line between the last two scans.

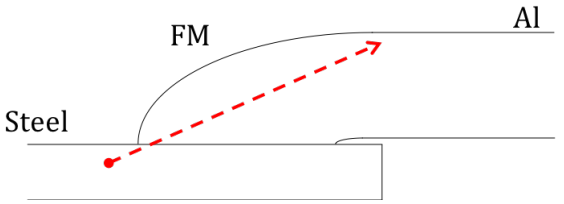

(a) Schematic representation of the position of the line scan over the sample surface.

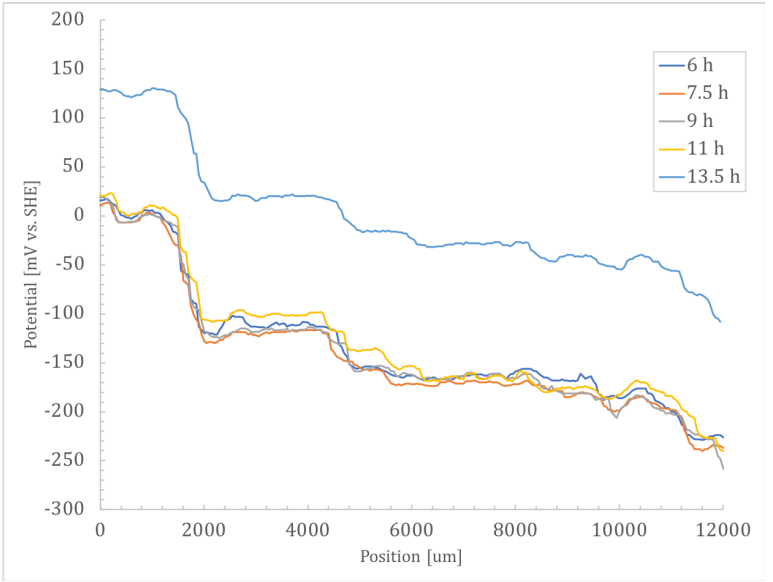

(b) Potential versus distance along the line.

Figure 4.28: Potential as a function of position along the line.

Surface Scans

The 3D scan in figure 4.29 show the distribution of the potential over the surface of steel, filler material and aluminium and further confirms the results from the line scans.

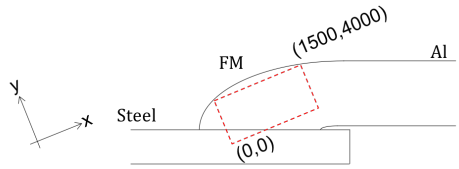

(a) Schematic representation of the area scanned over the sample surface.

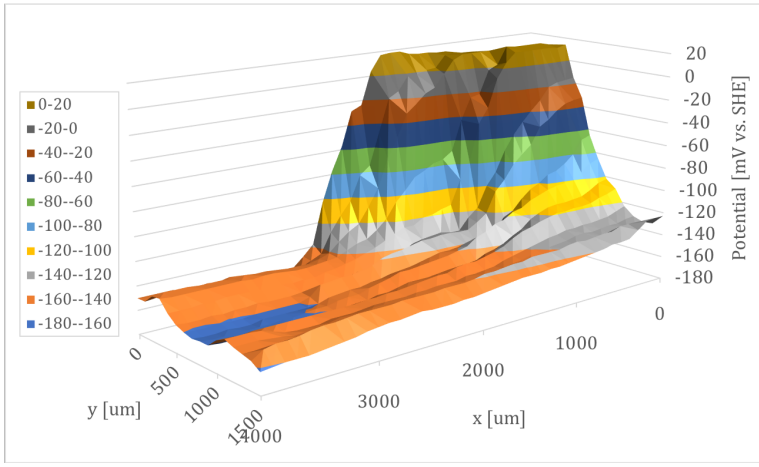

(b) 3D-plot of the surface scan.

Figure 4.29: Potential distribution over the scanned area.

Chapter 5

Discussion

5.1 Precipitation Hardening

Hardness measurements indicate that the heat treatment that has been performed in this work resulted in the desired temper conditions. The aluminium plates were received in the T1 condition which is as-extruded and naturally aged and homogenized. After solution heat treatment a reduction in hardness was registered for both alloys. The microstructure of the 6063 alloy consisted of an equiaxed grain structure and was subjected to some grain growth after SHT. The 6082 alloy, on the other hand, had a fibrous microstructure that was maintained after SHT except for a small recrystallized layer. Both alloys suffered from a reduction in hardness of about 20 HV after SHT. The drop in hardness is associated with the dissolution of hardening precipitates into supersaturated solid solution.

After an hour of precipitation hardening, the under-aged T6x condition was achieved. The hardness of the 6082 alloy was already higher than the T1 condition while the 6063 alloy was below its initial hardness. This indicates that precipitation takes place faster in the 6082 alloy.

Finally, after 5 hours the peak aged, T6 condition was reached and both alloys were harder than in T1 condition. It was not verified that this actually was peak hardness for the two alloys, but the procedure used for the precipitation heat treatment was referred to as standard practice by Hydro. The hardness that was achieved was 108 $\pm$ 3 HV and 87 $\pm$ 4 HV for 6082-T6 and 6063-T6, respectively. Compared to EN485-2 [59], standard for mechanical properties of aluminium alloys, the hardness that was achieved is in accordance with the standard which is given as 100 HV and 80 HV for 6082-T6 and 6063-T6, respectively.

5.2 Welding

Welding by CMT was performed with the same pre set welding parameters for all samples. Three of the welded samples resulted in sound welds and no problems were ex-

perienced. Problems occurred when the AA6082-T6x plate was welded and large dimples appeared in the filler material. This weld had to be discarded and welded with new plates was reattempted. Due to a limited number of plates, the welding parameters couldn't be experimented with. It was also desired to keep the welding parameters constant. On the second attempt, the weld still contained some dimples, but not to the same extent as for the first attempt. It was decided to keep this, and the result of this is further discussed in the section on tensile testing.

5.2.1 Effect of welding on hardness

Hardness distribution over the welds was measured and the results indicated that the heat input from CMT welding has had an effect on the mechanical properties of the weld. The hardness of the base material was reduced by up to 40 % due to welding for the AA6082-T6 alloy. The heat during welding was not recorded, but is above the melting temperature of aluminium. This means that the base material has been subjected to a temperature gradient. Closest to the weld, the base material is reverted to its SHT condition where strengthening precipitates are dissolved. With increasing distance from the weld, the hardness increases gradually towards the alloy's initial hardness value. This gradual increase is connected with the growth of hardening precipitates which decreases with decreasing temperature.

Across all four weld samples, the filler material is the softest with a hardness between 50 - 60 HV1 which is expected with its as-cast microstructure. This is slightly softer than the AA6063-T6x sample at 63 HV1 and from the hardness distribution of this weld, it can be seen that there is no apparent HAZ where the hardness of the base material has been reduced due to welding. This sample is, therefore, the one with the best match between the filler material and base material in terms of strength. For the T6 condition of the same alloy, the base material has a hardness of 87 HV1 and the hardness distribution shows a more apparent HAZ of about 12 mm where the hardness of the base material has been reduced due to the heat input from welding.

In the 6082 welds, the effect of welding on hardness is even more evident. The filler material has a hardness of 50 - 60 HV1 with an increase up to 76 HV at the interface between filler- and base material for both temper conditions. Moving into the base material, a drop in hardness corresponding well with the alloy's hardness in SHT condition is referred to as the HAZ. The width of the HAZ is measured as the distance into the base material where the hardness has reached the same level as measured for the base materials in its respective temper condition before welding. The HAZ is 11 mm and 13 mm for the T6x and T6 condition, respectively.

The hardness of the steel base material was measured to 211 HV1, and this is matching well with the hardness measured for all welds as expected. However, some scatter was observed below the fusion zone. These results are somewhat ambiguous whereas in the AA6063-T6x and AA6082-T6x samples all of the three hardness series shows a drop in hardness while for the AA6082-T6 sample, all series shows an increase in hardness. For the AA6063-T6 sample, the bottom series shows a drop in hardness while the series at the top, closest to the fusion zone, shows an increase in hardness. It is not readily explained what has caused this effect in the steel. No microstructural changes can be identified and the welding parameters were the same for all four samples.

5.2.2 Effect of welding on microstructure

Investigation of the microstructure in the weld show no indications of microstructural changes due to welding. No grain growth can be identified in the same area as where the HAZ was observed by hardness measurements. This further confirms that the loss in strength due to welding is attributed to growth or dissolution of hardening precipitates and is not caused by grain growth.

The filler material consists of an as-cast structure with large grains of α-aluminium and a continuous phase structure. Aune et.al.[29] referred to this structure as a eutectic phase. Based on the chemical composition of the filler material this eutectic structure may to contain iron, magnesium, silicon and also some copper and zinc. The composition of these two phases will be further discussed in the SEM section. A high pore density was also observed in the filler material of all four welds. This porosity could be caused by humidity in the filler material, gas pores, shrinkage porosity or zinc evaporation during welding. Earlier work has also found that zinc tends to be trapped in the filler material especially in the weld toe [29]. This is also further discussed in the SEM section.

On the interface between the aluminium filler material and steel, an intermetallic compound layer has formed as expected with fusion welding. Based on literature this IMC layer is assumed to be an Al_xFe_y-compound and the thickness of the layer was measured to 3- 4 μm is uniform across the whole bonding line length. This narrow IMC layer thickness is expected in accordance with the low heat input and also below the critical limit for maintaining mechanical properties which is referred to as 5-10 μm by Madhavan et.al.[28].

It was observed that the heat from welding had an influence on the hardness of the steel base material. Based on the comparison of micrographs taken in the steel below the fusion zone and the steel in mid-thickness of the plate, no change in microstructure can be seen to explain the effect the welding has had on the hardness. The three series of hardness measurements were carried out as identical as possible and the same indentation pattern was used for all four welds. However, the position of the pattern with respect to the top and bottom of the plate may have shifted a few μm in the horizontal direction. This can be a source of error and may explain the ambiguous hardness values measured in the steel below the fusion zone.

5.2.3 Effect of welding on the zinc coating

On the steel plate, an area with a width of 1 mm was found to be left as bare uncoated steel after welding. The zinc coating has most likely melted or even evaporated and subsequently been propelled away from the plate by the shielding gas. It is also believed that the same has happened to the zinc under the filler material, but the zinc hasn't been able to escape and have rather been mixed into the filler material. This theory is also supported by the literature which reports zinc rich zones in the filler material of similar welds [29, 47, 6]. This is further discussed in the EDS section.

5.3 Accelerated Corrosion Testing

5.3.1 Potential evolution during test

During the first eight hours of the corrosion test, the open circuit potential was stable at -1040 $mVvs.SCE$. This potential is in the same range as the corrosion potential of zinc in flowing sea water which is given as -1030 $mVvs.SCE$ [42]. This indicates that the zinc is acting as the anode in this galvanic coupling during the first eight hours, and as soon as the zinc is completely corroded away, the potential suddenly increases and stabilizes at a mixed potential between aluminium and steel at -730 $mVvs.SCE$. The corrosion potential of low alloy steel and aluminium is -610 $mVvs.SCE$ and -790 $mVvs.SCE$, respectively. It should be noted that the potential values presented from the theoretical background are measured in flowing seawater at 24 $°C$. Parameters such as temperature, flow rate, surface areas of the galvanic coupling, pH and type of electrolyte will vary the potential. Taken this into consideration, the values obtained during the test still corresponds well with the theory.

5.3.2 Effect of corrosion on bond strength

Tensile tests before, during and after corrosion testing indicates that corrosion is detrimental on the bond strength between the aluminium filler material and steel plate in the weld. Especially the first eight hours in this particular test solution seems to be the most decisive and detrimental.

Before corrosion, the fracture occurred in the filler material on the interface to the base material for the three sound welds. Compared to the hardness measurements, the area of fracture corresponds to the HAZ of the weld. After eight hours of corrosion, the failure mode changed and fracture occurred along the bonding line between the aluminium filler material and steel base material at considerably lower loads. This was also reported in the findings of Le Bozec et.al.[48].

During the corrosion test, the dissolution of zinc could readily be seen on the sample surfaces together with heavy gas development. This gas development is attributed to the cathodic reaction, being either oxygen reduction or hydrogen evolution. Hydrogen evolution is assumed to be an important cathodic reaction in such sour environments (pH 3). After eight hours of exposure, the gas development diminished and no zinc could be seen left on the steel surface. This is further supported by the potential that was monitored during the test. At the same time that no zinc could be observed left on the steel surface and the gas development diminished, the potential made a sudden increase. Two samples of each weld were collected and the effect of zinc corrosion was investigated by tensile testing. Tensile tests performed after eight hours indicates that the zinc corrosion has resulted in a loss of bond strength between the aluminium filler material and steel plate. The strength was reduced by up to 52 % compared to the maximum load before corrosion testing. This indicates that initially, the bond was stronger than the strength of the HAZ. During eight hours of immersion in the corrosive electrolyte, the corrosion has deteriorated the bond between steel and aluminium filler material resulting in a bond strength that is weaker than the HAZ.

After a total of 48 hours of exposure, the results show that two of the welds has continued to lose strength, while two of the welds shows an increase in strength. By comparing the size of the surface contact area between the aluminium filler material and steel, it can be seen that this has been reduced for all four samples during the 40 hours of immersion. However, the strength loss doesn't show a correlation between bonding surface contact area and strength. It should be kept in mind that each of the tensile tests was only tested with two parallels due to limited material availability. This is not a sufficient amount of parallels to produce good statistical data.

As previously mentioned, problems were encountered during welding of the AA6082-T6x. During tensile testing, this particular weld showed deviating behaviour compared to the other three samples. This sample failed at a low maximum load compared to the other welds and the fracture occurred along the bonding between aluminium filler material and steel base material both before and after corrosion testing. This indicates that the problems experienced during welding resulted in a poor weld where the initial mechanical strength of the bond was not good enough. Regardless of this, a reduction in strength was observed due to corrosion for this weld as well.

In Figure 5.1, the strength loss for all four samples are compared. Based on the initial maximum load before corrosion, the AA6063 welds were slightly stronger than the AA6082-T6 sample and significantly stronger than the T6x sample, which proved difficult to weld. This indicates that the welding parameters used in this work were better suited for joining of AA6063. The optimization of welding parameters to achieve the best mechanical strength for each alloy is a study of its own. In this work, the welding parameters were kept constant due to two reasons. To reduce the number of parameters that may affect the corrosion resistance and also due to limited amounts of available steel plates.

By comparing the maximum load after eight and 48 hours, the results are somewhat ambiguous. Two of the samples shows a reduction while two shows an increase. Again, this can be explained by the lack of a sufficient amount of tensile test parallels. Taken this into account, it can be discussed that regardless of initial strength, the strength of the welds after corrosion seems to level out with time regardless of alloy or temper condition. After exposure to the corrosion test, all welds fractured between the filler material and steel plate. The material combination in this area of interest is the same for all samples with AlSi5 filler material and the dual phase steel plate. It is likely to believe that this explains why the strength of the welds reaches the same level after 48 hours of testing. If this is true, the corrosion resistance of such joints is independent of the aluminium base material. Due to a limited amount of tensile test parallels, no conclusion can be made, but further studies should focus on filler materials selection. It could also be relevant to perform the same test for a longer time period with more tensile test parallels to confirm this theory.

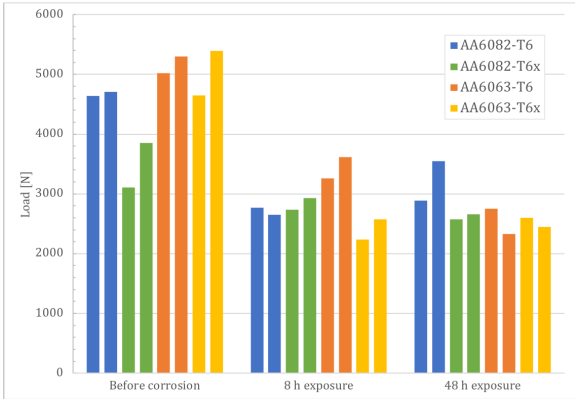

Figure 5.1: Comparison of strength loss versus time for all four welded samples. Both test parallels are presented.

5.3.3 Characterization of corrosion attacks

After 48 hours of corrosion testing, the corrosion attacks on welded samples were examined in LOM. Different corrosion attacks were observed across the different aluminium base materials and temper conditions.

The most apparent corrosion attacks were found on the AA6063-T6x sample. Pitting corrosion could be identified by visual inspection of the aluminium plate. The intensity of pits was large close to the weld and decreasing with increasing distance from the fusion zone. This may indicate that the corrosion of the aluminium has been accelerated by the galvanic coupling to the steel and that there is an IR drop in the electrolyte that leads to a concentration of corrosion attacks close to the fusion zone. From the LOM images, the pits were found close to the weld zone, but further away the corrosion is characterized as local IGC. The same alloy in the T6 condition was also found to be susceptible to IGC, but the IGC attacks were more uniform and continuous. However, close to the weld zone, an area with a width of 10 mm is not corroded. This coincides with the overlap between the aluminium and steel plates.

Corrosion of the filler material is similar for the two temper conditions of the AA6063 samples. From the micrographs, corrosion can be seen over the entire surface of the filler material with uniform depth. However, this is not uniform corrosion, but can be characterized as selective corrosion of a specific phase.

The most aggressive corrosion attacks have occurred at the end of the filler material closest to the steel plate which is further referred to as the weld toe. The corrosion attack has dissolved large amounts of the filler material and propagated along the interface between filler material and steel.

For the AA6082 samples, no local corrosion was found on the base material. Also, the filler material looks less attacked by selective corrosion than for the AA6063 samples, although the filler material that is used is the same across all four samples. Some corrosion was observed on the filler material for the T6x sample while the filler material on the T6 sample was unaffected of corrosion. However, the dissolution of filler material in the weld

toe was found to be most aggressive for the T6 sample. This indicates that when the base material is not susceptible to corrosion, the more localized and aggressive the corrosion attack will become in the material closest to the steel plate, i.e. the filler material.

The aluminium base materials showed varying corrosion behaviour. The AA6063 base material was subjected to IGC attacks far away from the weld for both temper conditions. For the T6x condition, heavy pitting was observed close to the weld with decreasing intensity with increasing distance from the weld. The AA6082 base material was not subjected to corrosion for either temper conditions. For this sample, less corrosion was also observed in the filler material, but more aggressive corrosion attacks can be seen in the weld toe. The corrosion behaviour observed in this study is not entirely in correspondaece with the results presented by either Svenningsen et.al.[45] or El-Menshawy et.al.[46]. The deviation may be explained by the welding. The materials in this study are welded and exposed to heat after precipitation heat treatment. Thus, the heat input will alter the temper condition and thus the corrosion behaviour of the base materials close to the weld.

5.3.4 Element analysis in EDS

The area around the weld toe showed large corrosion attacks for all welded samples and this area was further examined on uncorroded samples in SEM. From the backscatter electron image of the interface between aluminium filler material and steel, at least three phases are distinguishable by atomic number contrast. Phases with a high mean atomic number appear as light while phases with a lower mean atomic number appear darker.

The steel side looks unaffected of the welding and contains mainly iron. This particular steel is a low alloy steel, and other alloying elements is hard to identify with EDS analysis which is a qualitative analysis method rather than quantitative.

In the filler material, closest to the steel, a light grey area can be seen in the BSE image. This area is especially rich in zinc and this corresponds to the same area that was found to be heavily corroded in the LOM images.

Further into the aluminium filler material, two phases can be identified these were also observed in LOM. The EDS mapping and line scans were initially set up to map all of the alloying elements of the filler material, but the analysis showed that the filler material contained mainly aluminium and zinc. Based on the chemical composition of the filler material elements such as iron, magnesium, copper and silicon were also expected to appear. However, the EDS mapping showed insignificant quantities and no reliable patterns in the distribution of those elements. These elements were therefore left out of the analysis to remove clutter in the results.

It has already been discussed that the as-cast structure of the filler material contains a matrix of α-aluminium and a eutectic structure. This structure was found to be especially rich in zinc. The zinc-rich phase appears to be distributed as a continuous network inside the aluminium grains. This corresponds well with the observations of areas that were attacked by selective corrosion in the filler material. Microgalvanic corrosion is believed to have occurred in the filler material where it is likely to believe that the zinc-rich phase is less noble than the matrix.

The filler material originally contains 0.1 wt% of zinc and during solidification, the zinc may segregate to the grain boundaries and make up a eutectic phase. Also some of the zinc, especially in the zinc-rich zones close to the steel, may originate from the zinc coating

on the steel plate. During welding, the temperature exceeds the melting temperature and also possibly the boiling point of zinc. This allows zinc to be mixed into the filler material during solidification, this has also been proposed by Aune et.al.[1]. This is likely the cause for the formation of the zinc-rich zones close to the steel. These zones has corroded with a high corrosion rate due to galvanic coupling to more noble materials. The detrimental role of zinc in the filler material was also reported by Wloka et.al.[47] and Shi et.al.[6].

5.4 Potential measurements with SKP

The potential values obtained from SKP is the surface potential in a humid atmospheric environment and is thus, not the same as the potential values obtained in the immersion corrosion test with acidified salt water. In immersed condition, the metals will be more active as the rates of the cathodic reactions are higher and consequently, the rate of anodic dissolution will be higher. This results in lower potentials than in atmospheric conditions. It should also be noted that the potential from corrosion testing was referred to SCE and SKP analysis to SHE. It was chosen not to convert them as the relative differences in each experiment was more relevant rather than comparing the two.

An increase in potential was observed in the last point scan of the steel base materials and as well as in the last line scan. The point scan increased by 120 mV and the entire line scan increased by 100 mV in the last measurement. It is probable that the potential increase is related to adsorption of water [50] and oxide formation [60]. Oxygen reduction will take place on the steel surface with steel dissolution as the anodic counter-reaction. The dissolution of metal leads to the formation of oxides and in time this will result in an increased anodic overpotential as observed. Hence, the increase in oxide thickness is expected to be accompanied by an increase in potential [52]. For aluminium, as data is missing for the final point measurement, results are not conclusive.

The corrosive properties of the areas where zinc-rich phases were located were further investigated in the SKP analysis. From the SEM image, it can be seen that the zinc rich zone is approximately 60 μm wide. However, the results from SKP line and surface scans don't indicate any phases with less nobility than the reference values obtained from point scans of each base material. This may be explained by the lateral resolution of the instrument which is defined by the diameter of the needle tip, which was 170 μm in this experiment. To identify the potential of these phases, modifications of the instrument or application of other scanning microscopy techniques with even better resolution needs to be applied.

5.5 Evaluation of test procedure

The accelerated corrosion test was performed in an electrolyte with pH 3. The application of such sour electrolyte was mainly to achieve corrosion attacks and identify relative differences within a reasonable time. For automotive application, the environment may be humid and contain a large amount of salts. In addition, some components may also be exposed to local sour environments that occur due to the deposition of "road mud", especially on uncoated components of the chassis.

5.6 Further work

Initially, the main goal of this work was to compare the corrosion resistance of the CMT samples with joints made by the HYB solid-state joining method of the same materials. Due to practical aspects around the CMT welding method, lap joints are the desired weld configuration. Currently, butt welding is the desired configuration in HYB, but HyBond introduced the idea of slot welding with HYB during the work with this master thesis. Slot welding with HYB is currently at an early stage, but initial testing and modification produced promising results as was presented in chapter 4.2. However, HyBond needed more plates for further testing and optimization before samples could be produced for corrosion testing. Due to a limited amount of the steel plates used in this project, HYB slot welded samples for corrosion testing couldn't be produced within the time span of this master project.

It could be argued that any steel quality would have been sufficient for testing in this master project because the steel quality seems to be of less importance. No corrosion actually takes place on the steel base material as both the zinc coating and the aluminium will cathodically protect the steel from corrosion. However, it was desired to make joints of these particular materials since they are common in the automotive industry and relevant for the OPTIMALS project.

However, the OPTIMALS project goes on and the findings of this thesis should be used for further comparison with samples joined by HYB when more of the same materials are available. More steel plates of similar quality were sent from Benteler Automotive to SINTEF and the aluminium plates prepared for HYB joining was delivered to Professor Trond Furu.

In HYB joining the zinc coating on the steel is undesirable and will be removed by grinding in a small area in the fusion zone, corresponding to the area of the milled slot. By doing this, no zinc will be mixed into the filler material and the hypothesis is that the problems encountered with zinc rich zones in CMT welding will not be a problem in HYB. The zinc will then only serve its initial task, to protect the steel and also possibly the aluminium if submerged into an electrolyte with sufficient conductivity. This hypothesis should be further tested when HYB slot welded samples are produced.

Chapter 6

Conclusion

The objective of this study was to compare the corrosion behaviour of aluminium-steel welded joints made from CMT and HYB. Four CMT welds were produced from AA6063 and AA6082, both aged to T6x and T6 condition. The aluminium plates were welded to a zinc coated dual phase steel plate. Welded samples were tested in immersion corrosion testing and the welds were tensile tested before, during and after corrosion testing. HYB samples weren't produced for corrosion testing due to delivery issues of additional steel plates. Therefore, no comparison of the two methods can be made. However, the following conclusions on CMT welded samples can still be made from this work.

- Tensile testing revealed that the bond strength between aluminium filler material and steel was drastically reduced during the first eight hours of testing when zinc corrosion was the dominant reaction.
- The zinc coating has been applied to the steel for corrosion protection and for better wettability during welding. However, zinc was found to be detrimental for the corrosion resistance of these joints. Zinc has been mixed into the filler material during welding and this has produced zinc rich zones. In addition, the continuous phase structure found in the filler material was also containing zinc. These zones and phases were found to selectively corrode and result in a reduction in bond strength between steel and aluminium.
- In addition, the dissolution of zinc rich phases leaves an undesirable crevice underneath the filler material. This may result in further corrosion, reduction in bonding surface area and ultimately, complete lack of bonding.
- The corrosion behaviour of the AA6082-T6 base material was found to be superior to the AA6063 alloy in both temper conditions.

When HYB slot welding samples are produced, corrosion testing by the same procedure performed in this work should be carried out. The findings from the present work can then be used as a basis for comparison of the corrosion resistance of the two methods.

References

[1] O.M. Akselsen and X. Ren. *Arc welding of aluminium to other metals for light weight applications*. SINTEF, 2007.

[2] W.S. Miller, L. Zhuang, J. Bottema, A.J. Wittebrood, P. De Smet, A. Haszler, and A. Vieregge. *Recent development in aluminium alloys for the automotive industry*, volume A280. Materials Science and Engineering, 2000.

[3] R.P. Krupitzer. Steel is up to the automotive challenge. `http://www.machinedesign.com/metals/steel-automotive-challenge`, 2012.

[4] M. Goede, M. Stehlin, L. Rafflenbeul, G. Kopp, and E. Beeh. *Super Light Car—lightweight construction thanks to a multi-material design and function integration*. European Transport Research Review, 2008.

[5] K. Martinsen, S.J. Hu, and B.E. Carlson. *Joining of dissimilar materials*. 64. CIRP annals - Manufacturing technology, 2015.

[6] Y. Shi, J. Li, G. Zhang, J. Huang, and Y. Gu. *Corrosion behaviour of Aluminium-steel Weld-brazing Joint*, volume 25 of *5*. Journal of Material Engineering and Performance, 2016.

[7] U.F. Aakenes. *Industrialising of the Hybrid Metal Extrusion and Bonding (HYB) method - from prototype towards commercial process*, volume 339. NTNU, 2013.

[8] W.D. Callister and D.G. Rethwisch. *Material Science and Engineering*. Wiley, 8th edition, 2011.

[9] H.K.D.H. Bhadeshia and Sir Robert Honeycombe. *Steels, microstructure and properties*. Butterworth-Heinemann, Oxford, third edition, 2006.

[10] R. Kuziak, R. Kawalla, and S. Waengler. *Advanced high strength steels for automotive industry*, volume VIII of *2*. Archives of civil and mechanical engineering, 2008.

[11] Automotive steel definitions.
http://www.worldautosteel.org/steel-basics/automotive-steel-definitions/.

[12] M. Shome and M. Tumuluru. *Welding and Joining of High-Strength Steels (AHSS)*. Woodhead Publishing, Elsevier, 2015.

[13] G. Rosenberg, I Sinaiová, and L'. Juhar. *Effect of microstructure on mechanical properties of dual phase steels in the presence of stress concentrators.* A 582. Material Science & Engineering, 2013.

[14] World Auto Steel Association. Future steel vehicle results and reports.
http://www.worldautosteel.org/projects/future-steel-vehicle/phase-2-results/, 2018.

[15] J.K. Solberg. *Teknologiske metaller og legeringer*. NTNU, 2014.

[16] I.N. Fridlyander, V.G. Sister, O.E. Grushko, V.V. Berstenev, L.M. Sheveleva, and L.A. Ivanova. *Aluminium alloys: Promising materials in the automotive industry*, volume 44. Metal Science and Heat Treatment, 2002.

[17] J.R. Davis. *Aluminum and aluminum alloys*. ASM specialty handbook. ASM International, 2001.

[18] A.K. Gupta, D.J. Lloyd, and S.A. Court. *Precipitation hardening in Al-Mg-Si alloys with and without excess Si*. Materials Science and Engineering, 2001.

[19] Hydro Extrusions. 6063 alloy.
https://www.hydroextrusions.com/en-GLOBAL/why-aluminium/the-material/the-right-alloy/6063-alloy/, 2018.

[20] Hydro Extrusions. 6082 alloy.
https://www.hydroextrusions.com/en-GLOBAL/why-aluminium/the-material/the-right-alloy/alloy-6082/, 2018.

[21] Hydro Extrusions. 6082 aluminium.
https://www.hydroextrusions.com/en-GLOBAL/locations/north-america/united-states/local-content/extruded-aluminum-products/aluminum-extrusion-alloys/6082-aluminum/, 2018.

[22] MatWeb Material property data. Aluminium alloy heat treatment temper designations.
http://www.matweb.com/reference/aluminumtemper.aspx, 2018.

[23] ASM International Handbook Committee. *ASM Handbook, Volume 04 - Heat Treating*, volume 4. ASM International, 1991.

[24] J. Grønvold, T. Furu, and O. Lunder. *The Effect of Deformation on Intergranular Corrosion of AlMgSi Alloys*. Master thesis, Institute of Chemical Engineering and Biotechnology, NTNU, 2017.

[25] J.R. Davis. *Corrosion of Weldments*. ASM International, 2006.

[26] M.M. Atabaki, M. Nikodinovski, P. Chenier, J. Ma, M. Harooni, and R. Kovacevic. *Welding of aluminium alloys to steels: An overview*, volume 2 of *14*. J. manuf. sci. prod., 2014.

[27] L. Agudo, D. Eyid, C.H. Schmaranzer, E. Arenholz, N. Jank, J. Bruckner, and A.R. Pyzalla. *Intermetallic FexAly-phases in a steel/Al-alloy fusion weld*, volume 4205-4214 of *42*. Journal of Material Science, 2007.

[28] S. Madhavan, M. Kamaraj, and L. Vijayaraghavan. *Microstructure and mechanical properties of cold metal transfer welded aluminium/dual phase steel*. Taylor & Francis, 2016.

[29] R. Aune, E. Pettersen, and X. Ren. *Interfacial microstructure and mechanical properties of aluminium-zinc-coated steel joints made by CMT welding*. SINTEF, 2017.

[30] Guy Murry and Dominique Kaplan. *Traditional Welding Processes*. ISTE, 2010.

[31] Ø. Grong. *Recent Advances in Solid-State Joining of Aluminium*, volume 91(1). Welding Journal, 2012.

[32] EN 1011-1:2009. *Welding - Recommendations for welding of metallic materials - Part 1: General guidelines for arc welding.* European Standard, 2009.

[33] Y.M. Zhang. *Arc Physics of Gas Tungsten and Gas Metal Arc Welding, ASM Handbook, Welding Fundamentals and Processes*, volume 6A. ASM International, 2011.

[34] S. Selvi, A. Vishvaksenan, and E. Rajasekar. *Cold metal transfer (CMT) technology - An overview*. Defence technology, 2017.

[35] K. Mehta. *Advanced Joining and Welding techniques: An Overview*. Springer, 2017.

[36] K. Mori, N. Bay, L. Fratini, F. Micari, and A.E. Tekkaya. *Joining by plastic deformation*. CIRP Annals - Manufacturing Technology, Elsevier, 2013.

[37] J.E. Gould. *Mechanisms of Bonding for Solid-State Welding Processes, ASM Handbook, Welding Fundamentals and Processes*, volume 6A. ASM International, 2011.

[38] U.R. Aakenes, Ø. Grong, and T. Austigard. *Application of the hybrid metal extrusion & bonding (HYB) method for joining of AA6082-T6 base material*. Material Science Forum, 2014.

[39] E. Bardal. *Korrosjon og korrosjonsvern*. Tapir akademisk forlag, 1994.

[40] M.G. Fontana. *Corrosion Engineering*. McGraw-Hill Book Company, 3rd edition, 1987.

[41] K. Nisancioglu. *Corrosion Basics and Engineering Part I: Basic principles, compendium*. Norges Tekniske Høgskole, 1994.

[42] R. Baboian. *Galvanic corrosion, ASM Handbook, Corrosion: Fundamentals, Testing and Protection*, volume 13A. ASM International, 2003.

[43] K. Nisancioglu. *Corrosion Basics and Engineering Part II: Corrosion types, compendium*. Norges Tekniske Høgskole, 1994.

[44] G. Svenningsen. *Intergranular Corrosion of AA6000-Series Aluminium Alloys*. Doctoral thesis 2005:47. NTNU, 2005.

[45] G.Svenningsen, M. H. Larsen, J. C. Walmsley, J. H. Nordlien, and K. Nisancioglu. *Effect of artificial aging on intergranular corrosion of extruded AlMgSi alloy with small Cu content*, volume 48(6). Corrosion Science, 2006.

[46] K. El-Menshawy, A. A. El-Sayed, M. E. El-Bedawy, H. A. Ahmed, and S. M. El-Raghy. *Effect of artificial aging on intergranular corrosion of extruded AlMgSi alloy with small Cu content*, volume 54. Corrosion Science, 2012.

[47] J. Wloka, H. Laukant, U. Glatzel, and S. Virtanen. *Corrosion properties of laser beam joints of aluminium with zinc-coated steel*, volume 49. Corrosion Science, 2007.

[48] N. LeBozec, A. LeGac, and D. Thierry. *Corrosion performance and mechanical properties of joined automotive materials*, volume 5 of *63*. Materials and Corrosion, 2012.

[49] M. Rohwerder. *The Kelvin Probe Technique as Reference Electrode for Application on Thin and Ultrathin Electrolyte Film*. Springer, 2013.

[50] A. Nazarov and D. Thierry. *Rate-determining reactions of atmospheric corrosion*, volume 49 (2717-2724). Electrochimica Acta, 2004.

[51] M. Rohwerder and F. Turcu. *High-resolution Kelvin probe microscopy in corrosion science: Scanning Kelvin probe force microscopy (SKPFM) versus classical scanning Kelvin probe (SKP)*, volume 53(2). Electrochimica Acta, 2007.

[52] Ö. Özkanat, B. Salgin, M. Rohwerder, J.M.C. Mol, J.H.W de Wit, and H. Terryn. *Scanning Kelvin Probe Study of (Oxyhydr)oxide Surface of Aluminum Alloy*, volume 116 (1805-1811). The Journal of Physical Chemistry, 2012.

[53] P. Schmutz and G. S. Frankel. *Characterization of AA2024-T3 by Scanning Kelvin Probe Force Microscopy*, volume 145. Journal of the Electrochemical Society, 1998.

[54] ISO 18273:2015. *Welding consumables. Wire electrodes, wires and rods for welding of aluminium and aluminium alloys. Classification.* Norsk Standard, 2015.

[55] NS-EN 10346:2015. *Continuously hot-dip coated steel flat products for cold forming Technical delivery conditions*. Norsk Standard, 2015.

[56] Ø. Grong, Tor Austigard, and U. R. Aakenes. Possible use of the HYB method for lap & plug joining of Al-Fe plates - a feasibility study carried out for hydro aluminium in conjunction with Fredrik Heggeset Tranø's MSc thesis work. presentation, 2018.

[57] ASTM G85. *Standard practice for Modified Salt Spray (Fog) Testing*. ASTM International, 2011.

[58] Ø. Grong, Tor Austigard, and U. R. Aakenes. Testing of four Fe-Al slot welds produced using the HYB method - an exploratory study carried out for Hydro Aluminium in conjunction with Fredrik Heggeset Tranø's MSc thesis work. Presentation, 2018.

[59] EN 485-2. *Aluminium and aluminium alloys - Sheet, strip and plate - Part 2: Mechanical properties*. European Standard, 2016.

[60] R. Posner, O. Ozcan, and G. Grundmeier. *Water and Ions at Polymer/Metal Interfaces*. Springer, 2013.

Appendix A

Processing of AA6063 and AA6082

In this appendix details about the process history of the aluminium alloys, received from Hydro ASA, are presented. Chemical composition, extrusion and homogenization parameters are presented in Table A.1, A.2 and A.3, respectively. In addition, a complete overview of the processing performed after the alloys were received are presented in Figure A.1.

Table A.1: Chemical composition of the aluminium base materials, given in wt%.

Alloy	Fe	Si	Mg	Mn	Cr	Cu	Zn	Ti	Ga	V
AA6063.60	0.184	0.520	0.646	0.012	0.001	0.020	0.006	0.011	0.011	0.005
AA6082.52	0.220	1.000	0.810	0.530	0.140	0.100	0.005	0.010	0.010	-

The materials were extruded at Raufoss to 210 mm wide profiles and 3 mm thickness. Extrusion parameters are given in Table A.2. All samples used in the present investigation are taken from the middle part (between front end and back end) of the extruded section. After extrusion the plates were homogenized and the homogenization parameters are given in Table A.3.

Table A.2: Extrusion parameters for the respective alloys used in the present study.

Alloy	Charge	Press	T_{billet} [°C]	v [m/min]	P_{max} [bar]
6063.60	7972	5	480	10	172
6082.52	7728	5	510	6	191

Table A.3: Process parameters used for homogenization of the respective alloys used in this study.

Alloy	Homogenization temperature [°C]	Heating rate [°C/h]	Holding time [min]	Cooling rate [°C/h]
6063.60	575	200	135	350
6082.52	580	100	180	300 - 350

The procedure for precipitation hardening for 6xxx-series used in the present project is given in table A.4.

Table A.4: Standard heat-treatment procedure to obtain T6x and T6 condition for 6xxx series aluminium alloys.

		Temperature [°C]	Rate [°C/h]	Time [min]	Cooling
Solution heat treatment		540	Preheated furnace	15	Quench in water
Precipitation heat treatment	**T6x**	185	200	60	Air cooling
	T6	185	200	300	Air cooling

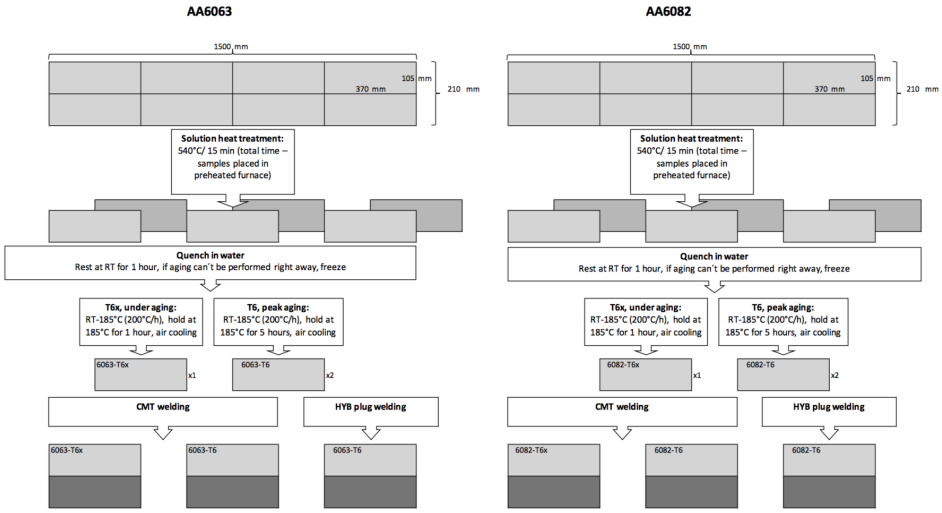

Figure A.1: Complete process route from the alloys were received to the welding.

Appendix B

Vickers hardness measurements

Average hardness values and their respective standard deviation are given in Table B.1. The values are based on five indentations made on the surface of each sample before, during and after the precipitation heat treatment procedure.

Table B.1: Vickers hardness (HV1) in the as received (T1), solution heat treated (SHT), under aged (T6x) and peak aged (T6) condition.

Alloy	Condition	Average hardness [HV1]	std.dev
6063	T1	68.6	1.1
	SHT	43.4	1.1
	T6x	62.8	2.8
	T6	86.8	4.1
6083	T1	81.4	1.7
	SHT	62.4	1.5
	T6x	91.2	1.8
	T6	107.8	3.2
HCT600		211.4	3.4